The Relationship between Frontal Dust Storms and Transient Eddy Activity in the Northern hemisphere of Mars as Observed by Mars Global Surveyor

Huiqun Wang[1], Richard W. Zurek[2], and Mark I. Richardson[1]
[1] Division of Geological and Planetary Sciences, California Institute of Technology, Pasadena, California, USA.
[2] Jet Propulsion Laboratory, California Institute of Technology, Pasadena, California, USA.

Abstract. We have compiled a catalog of frontal dust storms in the northern hemisphere using Mars Orbiter Camera daily global maps spanning ~2.3 Martian years of Mars Global Surveyor (MGS) observations (from 1999 to 2003). The most vigorous frontal storms that flush dust to the low latitudes occur in the fall and late winter, away from the northern winter solstice. While many streaks are observed in the polar hood during the winter solstice period, no frontal dust storms are seen in the vicinity of the north polar region. We have also analyzed simultaneous MGS Thermal Emission Spectrometer (TES) temperature data and found statistically significant negative temperature anomalies associated with frontal storms. In the lowest scale height of the atmosphere, the geographical and seasonal distributions of temperature standard deviations associated with transient variations agree well with the distributions of frontal storms. The correlation deteriorates with increasing altitude, suggesting that lower-level temperature waves are associated with the frontal dust storms. Specifically, eastward traveling m=3 waves with periods of 2-3 sols appear to be associated with flushing frontal storms.

1. Introduction

Dust storms are a major feature of Martian meteorology. With the advent of global and nearly continuous imaging of Mars with the Mars Global Surveyor (MGS) Mars Orbiter Camera (MOC), it has become possible to differentiate between different types of dust storms and study their distributions in detail. Published studies to date include those of Cantor *et al*. [2001], who documented the spatial, temporal and size distributions of all dust storms observed in 1999; Wang *et al*. [2003], who examined southward moving regional dust storms of 1999; and Strausberg *et al*. [2005], who documented the 2001 global dust storm. In this paper, we have analyzed ~2.3 Martian years of data for the northern hemisphere, focusing on a sub-type of dust storms (frontal dust storms) whose linear or curvilinear structure and movement resemble the classical cloudband structure of terrestrial wintertime storm fronts. Examples of such storms have been noted before from Hubble Space Telescope and MOC images [James *et al.,* 1999; Cantor *et al*., 2001; Wang *et al*., 2003].

Based on their appearance, it has been assumed that frontal dust storms are the result of dust being raised from the surface by strong winds associated with the intensified pressure and temperature gradients in storm systems. The storm systems are probably generated by the baroclinic instability at the edge of the polar vortex. Dust is spread behind the moving front, helping to identify the larger storm system, but also being part of the airmass exported to lower latitudes.

The existence of baroclinic weather systems on Mars is expected from the general theory of atmospheric circulations for Earth and Mars, which are rapidly rotating planets with thin atmospheres driven strongly by heat exchange with the surface and subject to large seasonal variations due to the tilt of their rotation axis

[Zurek *et al*., 1992]. Numerical simulations for Mars indicate the development of baroclinic systems consistent with visual observations of cloud and dust variations [James *et al*., 1999; Wang *et al*., 2003] and with the pressure, temperature and wind variations observed at the surface by Viking Lander 2 (48°N) [*e.g.* Barnes *et al*., 1993; Collins et al., 1996; Wilson et al., 2002]. The vertical temperature structure in simulations can be used to examine energy conversion [Barnes et al., 1993; Wilson et al., 2002]. Wilson [2002] showed the latitude – height structure of the observed and simulated traveling waves, and stated that they were consistent with baroclinic instability.

The data available for this study take the form of Mars daily global maps derived from MGS MOC images and atmospheric temperature profiles derived from the MGS Thermal Emission Spectrometer (TES). The principal advantages of the MGS data sets are the systematic daily, global coverage for a period that spans more than two Martian years. Furthermore, the horizontal resolution and spatial coverage of the MOC wide-angle images reveal the frontal features and regional phenomena in which we are interested. However, TES data are limited to 12 – 13 orbital tracks per day and TES retrievals have limited vertical resolution. A hallmark of a baroclinically unstable wave would be a tilting of the vertical structure with height and longitude. As a result, it is difficult to resolve "frontal" structure with TES data. Nevertheless, MGS data provide the synoptic view unavailable from previous observations to further test simulation results. The vertical structure of simulated baroclinic waves and simple idealized baroclinic models suggest that most unstable waves tend to be localized near the surface. With TES data, we can examine whether the storms have their maximum amplitudes in the interior of the atmosphere or near the surface, and this is a vital clue. Also, TES temperature data provide the best characterization of the seasonally varying "background" atmospheric structure in which the traveling waves are embedded.

Here, we specifically focus on examining the correlation between frontal development observed in images and thermal perturbations at various levels in the atmosphere associated with traveling waves. At high latitudes one can think of the traveling waves as distortions of a more zonally symmetric latitudinal gradient of temperature, which can be represented mathematically as a series of waves (i.e., variations with longitude). This representation is particularly useful when examining the TES temperature data. It is still useful when describing the organized condensate and dust patterns seen in the visual observations of the polar regions, but once the storm (and its associated dust front) has moved away from the polar vortex, one is really dealing with a specific event and not a "wavetrain" at that particular latitude. In this paper, we ask whether there is any further observational evidence that the dust fronts are associated with baroclinic storm systems and, whether there are patterns in the timing and scale of the storm systems with dust fronts that can be related to the hemispheric temperature structure. In summary, the purposes of this paper are to:

1. Establish the seasonal variability of frontal dust storms based on MOC imagery, including the spatial scale and frequency of the storm systems in which they are embedded.

2. Use temperatures retrieved from TES orbital data to test the hypothesis that frontal dust storms are embedded in mid-latitude baroclinic storm (traveling wave) systems.

3. Examine the relationship between the seasonal variability of the frontal storms, of the transient waves in the atmosphere (i.e., compare seasonal variability of MOC imagery and TES temperature variability), and of the structure of the polar vortex (based on TES temperatures and estimates of "baroclinicity", the latter is based on theoretical guidance).

1.1 Overview of Past Work

Since dust storms and clouds reflect the meterological conditions under which they form and indicate atmospheric circulation patterns, they have been studied extensively. For example, French et al. [1981] and Kahn [1984] documented the occurrence of different types of clouds using Mariner 9 and Viking images. Cantor et al. [2001] documented the occurrence of dust storms in 1999 using MGS MOC images. Previous classification of dust storms is mainly according to their sizes and positions, while this study classifies them according to their morphology and focuses on a particular type – frontal dust storm that resembles terrestrial baroclinic front. Some frontal storms develop into regional scale and transport dust from the north polar vortex edge southward to the low latitudes as they propagate eastward. These "flushing" storms generally occur in two seasonal windows Ls 200 – 240 and Ls 300 – 340 [Cantor et al., 2001; Wang et al., 2003]. This paper provides detailed description of the distribution of frontal dust storms including flushing storms. Wang et al. [2003] studied the mechanism of flushing storms with the Geophysical Fluid Dynamics Laboratory (GFDL) Mars General Circulation Model (GCM). Their results suggest that the synchronization between the low level winds in frontal systems and winds associated with the diurnal tide is key to the southward tracer transport. The seasonality of the simulated flushing storms is similar to that observed, though the simulation is under clear conditions year-round which contrasts the observed large increase of dust opacity in northern fall and winter. Newman et al. [2003] simulated a flushing storm in the Acidalia – Chryse channel using the Laboratoire de Meteorologie Dynamique (LMD) Mars GCM. In addition to MGS MOC, MGS TES and Mars Orbiter Laser Altimeter (MOLA) also provide simultaneous dust storm and cloud observations. Smith et al. [2004] documented TES observations of dust and water ice optical depth. This is particularly useful for studying the evolution of background dust and regional / global scale dust storms and clouds. Neumann et al. [2003] documented two Mars years of clouds detected by the MOLA. Their results show that absorptive clouds in the northern hemisphere minimizes around northern winter solstice.

The literature contains quite extensive discussions of transient / baroclinic eddies in the Martian atmosphere. Barnes [1980, 1981] demonstrated that highly coherent pressure, wind and temperature perturbations observed by Viking Lander 2 (48°N, 226°W) were consistent with eastward traveling baroclinic waves, centered to the north of the lander. Barnes [1984] studied linear baroclinic instability for the Martian atmosphere. He found that zonal wave numbers 3 and 4 were the most unstable in the mid latitudes, and that the growth rate was substantially decreased under enhanced static stability (such as resulting from increased dust opacity during dust storms). Barnes *et al.* [1993] further studied transient baroclinic waves generated

by the NASA AMES GCM. They found strong transient baroclinic eddies characterized by zonal wave number of 1–4 and periods of 2–10 days in the extratropics of the northern hemisphere during northern autumn, winter and spring. Hollingsworth *et al*. [1996] found enhanced temperature variance in Acidalia, Arcadia, and Utopia, and suggested that these Martian storm zones were controlled by the topography. Hollingsworth *et al*. [1997] further studied the seasonal cycle of storm zones on Mars, and found that Martian storm zones could occur in northern autumn, winter and spring, with the springtime variance being the strongest.

Wilson *et al*. [2002] identified a fast (6 – 7 sol) and a slow (~20 sol) eastward traveling zonal wave number m=1 in the mid level air temperatures in the northern hemisphere of Mars using MGS TES data. They simulated traveling waves using the GFDL Mars GCM, and stated that simulations typically yield traveling waves of zonal wave 1, 2 and 3 with periods of 7, 3-4, and ~2 sols, respectively, which are consistent with Viking lander observations and modeling work by Barnes et al. [1993]. They also pointed out that the simulated waves 2 and 3 are shallow features, and all the "fast" waves have temperature maxima at low levels (at the steering level), a westward phase tilt with height, features which are consistent with baroclinically unstable waves. Banfield *et al*. [2004] cataloged the behavior of different modes of transient waves in TES data. They found that m=2 and m=3 were confined nearer the surface than m=1. They also found that in the northern hemisphere, m=2 and m=3 were more evident in the fall and spring, while m=1 dominated the period around northern winter solstice.

While much work has been done studying observations and models of transient wave activity, the linkage between these waves and observed fronts is much weaker, and the current paper is an attempt to fill this gap. In the next section, we first discuss the identification of dust fronts in the MOC data, providing examples, then present statistics on the seasonal and spatial distribution of fronts over the course of two Martian years. In Section 4, we examine the correlation between the seasonal and spatial patterns of dust front development and of transient wave activity. Having provided some evidence of this correlation, in Section 4.4, we attempt to explain the relationship between the seasonal variation of frontal development and the seasonal variation of the structure of the polar vortex

2. Mars Orbiter Camera data and Frontal Storm Identification

In this study, we employed both MGS MOC and TES data. The analyzed data covered the period from June 1999 (L_S~150º) to September 2003 (L_S~270º), corresponding to ~2.3 Martian years. MGS is in a 2-hour, nearly sun-synchronous, and nearly circular mapping orbit [Albee *et al*., 2001]. During the course of each orbit, the MOC wide angle push-broom cameras built a pair of global map swaths in red and blue filters at a resolution of roughly 7.5 or 3.75 km/pixel (depending on across-track summation mode) [Malin and Edgett, 2001; Cantor *et al*., 2001; Wang and Ingersoll, 2002]. At the same time, TES collected spectra from 200 to 1600 cm^{-1} (6–50 micron) at spectral resolutions of 10 or 5 cm^{-1}, usually oriented nadir, with surface resolutions of roughly 6-10 km, with six instantaneous pixels [Christensen *et al*., 2001]. TES data are used to study temperature perturbations associated with frontal storms, and are introduced in section 4.

Mars daily global maps were made from MOC global map swaths following the method described in Wang and Ingersoll [2002]. We have used these daily global maps to identify dust and/or condensate cloud bands, which appear similar to terrestrial baroclinic fronts. Examples of many of these different kinds of features are shown in Figure 1, which provides a visual definition for the concepts and feature categorizations used here, such as streak *vs.* front. With dust fronts identified on the basis of linear or curved band morphology, we assign a unique identification (ID) number to each identified feature, and record the position of the southern edge and the corresponding L_s. In this way, a catalog of frontal storm occurrence as a function of location and season has been built up. We have further sub-classified the features according to whether they were composed of dust or water ice (a categorization based on color), whether they showed apparent southward motion (*i.e.* for dust fronts whether the storm flushes dust southward), whether the feature was new or had been identified on previous days, whether the front was detached from the polar cap/hood edge, whether the front could have been related to topographic slope winds rather than a propagating front, and whether the front could have been a streak rather than a front. Fronts that were clearly persistent in the images for more than one day (multi-day events) were identified with the aid of animated daily global maps and were tagged with the same ID that was assigned when that feature was first identified. We continued to track such features even if the original frontal appearance was lost and regardless of the underlying drive for subsequent movement (the nature of which could generally only be speculated). For events that involved both dust and condensate clouds, we recorded the event as both a dust and an ice clouds event. Given that the identification of features in the images is a subjective process, we examined the images twice in the time order of collection, and once again with random time ordering (in order to minimize creeping changes in feature definitions and criteria). Only events that were recorded in all three passes through the data were included in the catalog.

Fig.1

3. MOC Frontal Storm statistics

Results from the first MGS mapping year (MY 24) of the MOC frontal storm survey are shown in Figure 2 (images from 1999 to 2001). The plotted data points correspond to the southern edges of dust fronts that are listed as new dust events in the catalog. The spatial distribution data show that most of the frontal dust storms were concentrated in the low topographic regions of Acidalia, Arcadia and Utopia. Using GCM simulations, Hollingsworth *et al.* [1996] has shown that these regions are storm zones in the northern hemisphere of Mars. The middle panel shows the latitudinal and seasonal distribution of frontal dust storms from late northern summer (L_s=150º) to the northern summer solstice of the next Martian year (L_s=90º). A striking feature in this plot is the absence of storms in a period centered on the northern winter solstice (L_s 240º-L_s 300º, solstice at L_s 270º). During the solstice period, many streaks such as those in Fig. 1e were observed in the polar hood, however, none showed any clear frontal features such as those seen in Fig. 1b, c and d. Away from the solstice period, the latitudes of frontal dust storms appear to follow the trend indicated by the terminator curve (latitude of the edge of polar night). Though we did not measure the size of the storm explicitly, the distance between the terminator and the southern edge of the storm can serve as a proxy for the meridional extent of the storm from early fall to mid winter. Note that the polar cap is very extensive in late winter and early spring. As a result, the extent of the polar cap is much larger than the extent of the polar night (Fig. 1f). In this case, the size of the

Fig.2

storm is better measured from the edge of the polar cap. Interestingly, the largest of the frontal storms that transported dust to the low latitudes (*e.g.* Fig. 1d) occurred just before and just after the no-storm period. We will refer to such large frontal dust storms as "flushing storms" [Wang *et al*., 2003]. The histogram of the occurrence data shows maxima during the periods L_s=160º-170º and 190º-230º. During the L_s=210º-230º period, repeated flushing storms transported dust from the northern hemisphere to the southern subtropics through the Acidalia–Chryse channel, and result in global impact on the atmospheric thermal structure in the first MGS mapping year [Wang *et al.,* 2003]. This activity was followed by an abrupt cessation of frontal storm activity. The occurrence frequency of storms shows a broad peak centered in late northern winter following northern winter solstice.

Occurrence data for the second MGS mapping year (MY25, 2001-2003) are shown in Figure 3. In this Martian year, a global dust storm developed, which originated near the Hellas basin around L_s~182º, peaked around L_s~210º, and dissipated by L_s~240º [Smith *et al*., 2002; Strausberg *et al*., 2005]. Despite the global dust storm, the data on frontal dust storm activity shows similar occurrence patterns in the geographical and seasonal distributions of frontal dust storms as those for the first MGS mapping year. Many fronts were observed around the north polar cap shortly after the onset of the global dust storm. The frontal storm shut-off date in this year (L_s~220º) is earlier than that in the previous year (L_s ~230º). The global dust storm caused ~30ºK warming at 0.5mb over 10 days after the storm onset, and ~40K warming at the peak of the storm compared to the previous year [Smith *et al*., 2002]. This global dust storm appears to have had a qualitative effect of pushing the pre-solstice atmospheric thermal state into that more typical of the solstice period, which is consistent with the earlier frontal storm shut-off for this year. In the early phases of the global dust storm, several dust fronts reached the mid latitudes, but no large flushing fronts were observed in the later part of the global storm. This may be due, on the one hand, to the fact that at the peak of the global storm, the very thick dust haze south of the northern polar region made it difficult to identify dust fronts in the low latitudes. On the other hand, increased static stability and the strengthened polar jet may have suppressed baroclinic storms.

Fig.3

The distribution of flushing dust fronts observed from 1999 to 2003 (MY24-26) is shown in Figure 4. This figure highlights the solstice gap in the seasonal distribution evident in all three years of MGS observations (and to this degree a robust feature). Large flushing storms generally occur during two windows, one at L_s=200º-240º and the other at L_s=300º-340º. These frontal storms can transport dust from the northern mid- and high-latitudes well into the low latitudes, and sometimes across the equator and into the southern mid-latitudes. Much less frequently, in early fall and early spring, large flushing storms can also transport dust to latitudes as low as ~25ºN. The majority of such flushing events occur in the Acidalia channel, but the other two low topographic channels, associated with Arcadia and Utopia, are also host to quite a number of flushing storms. In the pre-solstice period of Year 3, the most active channel was Utopia.

Fig.4

Examples of flushing fronts are shown in Fig. 5 for each of the three channels. Figure 5g shows a Utopia flushing dust storm that transported dust to ~25ºN at L_s~206º. It was one of a sequence of similar events. In the following week, dust was tracked to the equator. At L_s~212º, this dust was augmented by material lifted by

Fig.5

another dust storm, and eventually the dust reached northern Hellas. Figure 5f shows another flushing storm in Utopia, but at L_s~324º in Year 2. A representative flushing storm in Arcadia is shown in Fig. 5c. Arcadia dust fronts are usually orientated in a more north–south direction than those in the other two channels. Other panels in Fig. 5 show examples of Acidalia flushing dust storms in different seasons and years. White arrows in Fig. 5a, d, e and h point to dust patches/bands south of the main frontal bands. These are probably associated with dust flushed southward by previous flushing storms in the channel or perhaps, with newly lifted dust ahead of the original flushing storm [Wang *et al*., 2003].

4. Transient Eddies Observed by the Thermal Emission Spectrometer

Atmospheric vertical temperature profiles derived from the TES spectra are obtained from the Planetary Data System [Conrath *et al.,* 2000]. The temperatures are provided on 38 pressure levels between 16.582 mb and 0.0016 mb, and are stored in "ATM" tables as a part of the standard TES products. In order to test the fidelity of TES retrievals in the lower atmosphere, Hinson *et al.* [2004] compared MGS TES temperature profiles with nearly simultaneous MGS Radio Science (RS) occultation temperature profiles at the same locations. They found temperatures retrieved with the two instruments and techniques to agree to within ~2 K for pressures < 400 Pa, while TES temperatures at 610 Pa are generally ~2 – 8 K warmer than RS temperatures. Since perturbations of TES temperatures are relative temperature changes at fixed pressure level, the absolute temperatures are not so critical. Note that traveling waves have been found in both TES and RS data [Wilson et al., 2002; Banfield et al., 2004; Hinson and Wilson, 2002]. Since the RS data are temporally and spatially sparse, they are not suitable for the current study.

4.1. Temperature anomalies associated with flushing storms

By analogy with terrestrial weather systems, it would seem reasonable to hypothesize that the observed dust bands delineate fronts that are associated with instabilities in the atmosphere, and likely with baroclinic instability. This hypothesis suggests that the fronts should be directly related to thermal perturbations in the atmosphere, and specifically with the patterns of warm and cold sectors observed in terrestrial cyclones. In order to search for such temperature anomalies associated with frontal storms, we have calculated day-time temperature perturbations at each vertical level along the TES observation track. For each track on the day side, we first bin TES temperatures along the tracks by 1° latitude. A mean and standard deviation is constructed for each bin using all the data (at a given level) that lie within 15° longitude and 1° latitude of the bin center, and that are available for 50 MGS orbits (~100 hours) on either side of the bin center. The means are subtracted from the temperatures at the bin centers to get temperature anomalies. The significance of the anomaly is gauged by comparison with the standard deviation. An example for L_s~209º in Year 1 is shown in Fig. 6. Temperature anomalies at 4.75 mb along TES tracks are color coded and superimposed on polar stereographically projected Mars daily global maps (0ºN – 90ºN), which are composed using the global map swaths obtained from the same MGS orbits. The numbers next to the tracks are the 13 sequential track numbers from which this daily global map is constructed. Tracks 5 and 6 cut across the dust front indicated by the arrow. Large negative temperature anomalies are observed north of and behind the dust band, suggesting that dust is located within the cold sector behind or adjacent to a cold front. The extreme

Fig.6

temperature anomaly in this case is ~-20 K, and the corresponding standard deviation is ~-10 K. The temperature anomalies are largest near the surface and decrease with altitude. The anomalies become comparable to the standard deviations by 2.24mb, indicating that signatures of baroclinic storms were confined to the lower atmosphere.

We have summarized the 6.1 mb temperature perturbation results for flushing storms in Fig. 7. The horizontal axis is the extreme temperature perturbations (ΔT) along the tracks that cut across frontal dust storms. The vertical axis is the standard deviation of transient temperature perturbations for the bin into which that temperature falls over the 50 orbits range, as defined above. Note this figure contains much fewer data points than Fig. 2 and 3 because it does not include small frontal storms. The lines in Fig. 7 correspond to ±1 and ±2 standard deviations (σ). If a track shows only one extreme point (either positive or negative anomaly), the extreme point is recorded. In cases where a track shows both positive and negative anomalies, we do the following: if the absolute values of the anomalies are both larger or both smaller than the standard deviation, then the anomaly with the larger absolute value is recorded, otherwise, the one with the absolute value larger than the standard deviation is recorded. The 6.1 mb temperature anomalies (ΔT) associated with the flushing storms range between ±20K. The proportion of points within different sectors of Fig. 7 is summarized in the first row of Table 1. Points (ΔT) that lie outside of the sector between -σ and σ are above one standard deviation compared to natural transient temperature perturbations (T') in that bin (defined above). The second row of Table 1 lists the proportion expected for a Gaussian (random) process. The Table shows that 52% of the observed ΔT's lie below –σ, and 9% lie below –2σ. For comparison, in a Gaussian distribution, only 16% of data should lie below –σ, and only 2.3% should lie below –2σ. The mean of the recorded ΔT's is -3.84K, and the standard deviation of recorded ΔT's is 8.89K. There are n=147 data points in Fig. 7. A student's t-test with a null hypothesis H0: ΔT<0 (*i.e.* that there is negative temperature anomaly associated with flushing storms) gives:

Fig.7

$$X = \frac{\Delta T}{std(\Delta T)\times\sqrt{n-1}} = \frac{-3.84}{8.89\sqrt{147-1}} \approx -5.24 < -2.35$$

which is in the lower 1% quartile of a student's t-distribution with 146 degrees of freedom. Therefore, we accept the null hypothesis at a 1% significance level. This statistical analysis shows that there is a high degree of confidence that the observed data are consistent with cold temperatures being associated with flushing frontal storms. It should be noted that large overlying dust opacity can depress surface temperatures substantially (Wilson, personal communication). Therefore, it is possible that all dust events would be characterized by cold temperatures independent of the atmospheric circulation. However, in most cases, cold temperatures span the whole region north of the dust band, not just over the band itself (e.g. Fig. 6). So, it is reasonable that dust band is near the interface of cold and warm airmasses.

4.2. Seasonality of transient temperature perturbations and frontal storms

The baroclinic hypothesis for the development of visible fronts argues for a relationship between the behavior of these fronts as revealed in the frontal storm catalog and the distribution of transient eddies as revealed by TES thermal

measurements. To test this, we calculated transient temperature perturbation standard deviations for a range of seasonal dates. Banfield *et al.* [2004] have described traveling waves in the Martian atmosphere using MGS TES nadir data. We present similar analyses here, but with specific emphasis on their relationship to fronts. We calculated the standard deviation for daytime TES temperatures within grid boxes of 15° longitude by 2° latitude by 30° L_s. A 5th-degree polynomial temporal trend is removed from the time series at each gridbox before the standard deviation is calculated in order to remove slow seasonal temperature variation due to quasi-stationary waves.

The upper three panels of Fig. 8 show zonally averaged standard deviation of temperature at 4.75 mb as a function of latitude and L_s for MGS Year 1, 2, and 3 (MY 24 – 26). Stronger eddy activity is seen to have occurred before and after the solstice period. This pattern shows great similarity to that obtained for frontal dust storms observed in images (*c.f.* Figures 2, 3, and 4), suggesting that the meteorological systems associated with these fronts contribute significantly to the standard deviation of temperature. In the pre-solstice period, eddy activity is the weakest in the second mapping year, consistent with frontal activity being suppressed during the 2001 global dust storm. Stronger eddy activity is observed in the autumn of the third year than in the autumns of either of the previous two years. This is perhaps related to the overall weaker static stability in the pre-solstice period of the third year (see below and Fig. 9). We also counted more frontal storms in the autumn of the third year than in the previous two autumns (not shown). The lower three panels of Fig. 8 show zonally averaged standard deviation at 2.24 mb. The seasonal distribution of eddy activity at this level significantly differs from that for the frontal storms. The fact that the strong, double peaked pattern evident at the 4.75 mb level disappears at 2.24mb suggests that the eddies responsible for the lower level patterns (and by extension, the dust fronts) are confined to lower levels. Banfield et al. [2004] noticed very strong m = 1 traveling wave activity in the upper atmosphere (say 0.5mb) that peaks in the solstice season. Wilson et al. [2002] argues that it is a barotropic energy conversion and that the traveling waves are associated with inertially-unstable regions at low latitudes. We will discuss different wave modes evident in the TES data further in Section 4.4.

Fig.8

Figure 9 shows the seasonal distribution of several parameters related to baroclinic instability theory and derived from the zonal mean TES temperatures. The left column corresponds to 4.75 mb, and the right column corresponds to 2.24 mb. The top row shows the latitude of polar vortex edge which is defined as the latitude corresponding to the minimum latitudinal temperature gradient ($\frac{dT}{dy}$) between 30ºN – 80ºN. In general, the polar vortex is about 6º in latitude closer to the pole during the winter solstice period than it is during early/mid fall and mid/late winter. Row 2 shows $\frac{dT}{dy}$ at the vortex edge. The temperature gradient maximizes during L_s 260º – L_s 300º due to the enhanced polar radiative cooling and the mid-latitude adiabatic warming due to the descending branch of the Hadley circulation during the winter solstice period. The range of temperature gradient variation is larger at the upper level than at the lower level. Row 3 shows static stability parameter squared (N^{*2} is also the Brunt-Vaisalla frequency squared) at the vortex edge. It maximizes during L_s 230º – L_s 270º due to the greater poleward slope with height of the polar vortex boundary during the winter solstice period. The global dust storm in MGS Year 2 lifted the

Fig.9

atmospheric stability in the pre-solstice period over the other two years, especially at upper levels. MGS Year 3 has the smallest fall-time static stability in the three years. However, the winter-time stability in MGS Year 3 is substantially larger than the other two. This is associated with the regional dust storm in December 2003, before the landing of Mars Exploration Rovers (MER). Row 4 of Fig. 9 shows the baroclinic parameter ($\alpha = \frac{f\left(\frac{du}{dy}\right)}{N*} = \frac{R\left(\frac{dT}{dy}\right)}{N*H}$) at the vortex edge, where f is the Coriolis parameter, H is the scale height. The combined behaviors of $\frac{dT}{dy}$ in Row 2 and N^{*2} in Row 3 result in a more symmetric seasonal variation of the baroclinic parameter (α) which maximizes at the northern winter solstice. The baroclinic parameter is proportional to the growth rate of the most unstable baroclinic waves in the Eady model [Holton, 1992; Barnes et al., 1993]. The baroclinicity of the atmosphere is the strongest around northern winter solstice. However, eddies in the lower atmosphere are actually weaker during the solstice period. At upper levels, the strongest baroclinicity still occurs at L_s ~270º. While eddies in MGS Year 1 appear to be centered on the solstice, eddies in MGS Year 2 maximize during L_s 240º – 260º, and eddies in MGS Year 3 maximize even earlier than MGS Year 2. So, there is not much correlation at upper levels.

4.3. Flushing storms and storm tracks

Fig.10

Figure 10 shows the Latitude – Longitude distribution of transient temperature rms amplitude at 4.75 mb for selected 30° L_s periods of MGS Year 1 (MY 24). Figure 10a corresponds to the period before the formation of north polar hood. The vortex edge temperature gradient is sharpening as the northern fall approaches. Compared to the other panels in the figure, this period does not have much eddy activity between 0º and 76ºN. Figures 10c and d correspond to the solstice period. Images for this period show streaks in the polar hood, but no frontal storms (Fig. 1). This period has the strongest baroclinicity, but the weakest eddy activity in the lower atmosphere. Eddy activities are concentrated in a thin circumpolar band about 6° wide in latitude with a zonal wave number two pattern at the edge of the polar vortex. Figure 10b, e, and f correspond to the pre- and post- solstice periods when regional scale flushing dust storms transport dust from the northern mid / high latitudes to the low latitudes. Examples of such storms are shown in Fig. 5. Significant eddy activities apparently span a wider latitudinal band (~12° latitude in most places) in these periods. Moreover, large standard deviations are evident in/near low topographic channels, especially in Tempe Terra and Acidalia where most of the flushing storms are observed in MGS Year 1. Consistent with the large spatial scale of flushing storms, the spikes in standard deviations are also elongated in the north – south direction. The Acidalia sector appears like a storm zone due to the locally larger temperature variations. Hollingsworth et al. [1996] investigated Martian storm zones using NASA AMES GCM, and pointed out that topography played a dominant role in localizing transient eddy activity to Acidalia, Arcadia and Utopia. GCM results show strong transient baroclinic eddies during northern autumn, winter and spring, with the winter solstice storm zones being weaker [Barnes et al., 1993; Hollingsworth et al., 1997; Wang et al., 2003, Basu et al., manuscript in preparation]. Our study suggests that the largest enhancement of the localized transient temperature anomalies are associated with flushing storms which are the largest frontal dust storms.

A plot similar to Fig. 10 can be found in Fig. 20 of Banfield et al. [2004] for MGS Year 2 (MY25). Note that they plotted the area north of 10ºN. Their figure shows that strong storm zones are evident in Acidalia during mid to late northern winter. This is in nice agreement with the timing and location of the observed flushing storms. No such eddy activity centers are observed in the pre-solstice period when the global dust storm (in MGS Year 2, MY 25) dramatically increased the atmospheric static stability.

Figure 11 is similar to Fig. 10, but for MGS Year 3 (MY 26). Weaker eddies in the winter solstice period is sandwiched between stronger eddies in the fall and winter. In agreement with the elevated eddy activity in Utopia in the pre-solstice period, MOC observations show that flushing storms are especially active in the Utopia channel this fall. An example is shown in Fig. 5 and discussed in Section 3. We have yet to process images after L_s 270º in the third year to see what happened in the post-solstice period.

Fig.11

MGS observations show that the minimum in the seasonal cycle of eddy temperatures and frontal dust storms occur when the atmosphere is deemed more unstable to linear baroclinic instability. This is analogous to the terrestrial mid winter suppression of baroclinic wave activity in the Pacific [Nakamura, 1992; Chang, 2001]. Harnik and Chang [2004] found that the narrowing and strengthening of the jet could explain the decrease of spatial growth rate of baroclinic eddies with shear. Both observations and simulations for the Martian atmosphere show that the north polar jet is generally sharper and stronger during the winter solstice period [Banfield et al., 2003; Haberle et al., 1993], but a detailed quantitative assessment of these effects requires further study. In addition, understanding the conditions favorable for the development of flushing dust storms will greatly improve our understanding of Martian storm zones.

4.4. Wave Modes in TES data

We have used the same space – time decomposition as that in Banfield et al. [2004] to identify eastward and westward traveling waves. Figure 12 shows the power of eastward traveling waves with periods of 2-8 sols as a function of latitude and L_s for MGS Year 1 (MY 24). The upper row is for 4.75 mb, and the lower row for 2.24 mb. The three columns from left to right correspond to zonal wave number m = 1, 2, and 3 respectively.

Fig.12

The upper panels of Fig. 12 show that m = 3 wave is mainly responsible for the enhanced eddy activity in the lower atmosphere away from the solstice. In fact, the m = 3 waves have periods between 2 and 4 sols [Banfield et al., 2004]. Banfield et al. [2004] reported that the m = 3 wave speeded up from a period of 2.8 sols at L_s ~190º to a period of 2.2 sols during L_s 215º – 230º. Successive flushing storms were observed on a daily basis during L_s 215º – 230º in MGS Year 1, and resulted in a planetary-encircling dust storm after L_s 230º. Wang et al. [2003] argued that southward dust transport by baroclinic fronts could be facilitated if dust fronts transverse to Acidalia during the "open tidal gate" hours from 9AM to 7PM local solar time when the southward eddy circulation is in phase with the maximum southward component of the diurnal tide circulation. An m = 3 wave with a 2-sol period has a zonal wavelength of 120º, and travels around the pole at ~60º

longitude/sol. If the first baroclinic fronts associated with the wave happens to be in the low topographic channel during the "open gate" hours, there is a good chance that the next fronts will be a little late in local time but still within the "open gate" hours. This would argue that the 2.2-sol m = 3 wave is more efficient in generating successive flushing storms than m = 3 waves with longer periods. The m = 1 and 2 waves at 4.75 mb cover a larger latitudinal range away from the solstice, but the amplitudes show no obvious correlation with the transient temperature standard deviation plot of Fig. 8. Barnes et al. [1993] presented seasonal changes in baroclinic wave modes simulated by the NASA AMES GCM. Their results show that under clear conditions, the dominant mode at 4 mb is m = 1 at northern winter solstice, m = 2 in early autumn and m = 3 in late winter. Under very dusty conditions, their results show that m = 3 is dominant at 4 mb around the solstice. These GCM results show various similarities and differences with the observations.

The lower panels (2.24 mb) of Fig. 12 show that m = 1 dominates during L_s 230º – 300º, m = 2 dominates in early fall and late winter, and m = 3 is negligible. The shift to smaller zonal wave number at the solstice period is in qualitative agreement with the behavior predicted by simple models such as the Eady model [Barnes et al., 1993]. It is interesting to note that the spatial and temporal distributions of m = 2 on both pressure levels in Fig. 12 follow the curves for the polar vortex edge very well (first row of Fig. 9), consistent with the wave being associated with the sharp temperature gradient at the polar vortex edge. Figure 12 indicates that m = 3 was relatively close to the surface. Banfield et al. [2004] found that m = 2 and 3 were more evident in the fall and spring rather than in the winter solstice period, which was dominated by m = 1. They also found that m = 3 was confined to the lowest scale height. The vertical structure of zonal wave 1 is shown in Wilson et al. [2002]. They stated that the simulated waves 2 and 3 have a much shallower structure. (TES has difficultly showing this low-level structure). These results suggest that our observed frontal dust storms were associated with m = 2 or 3 eastward traveling waves in the lower atmosphere.

5. Summary

Long-term observations are invaluable to the study of the Martian atmosphere. The nearly continuous global atmospheric monitoring by MGS has provided us a great opportunity to study the spatial and temporal distribution of different types of clouds and dust storms. This paper summarizes more than two Martian years of observations of frontal dust storms in the northern hemisphere of Mars, and examines the relationship between the morphological features (of dust storms) observed in MOC images and the thermal signatures derived from TES temperatures.

Our results show the existence of cold temperature anomalies behind most dust fronts in the lowest scale height of the atmosphere. The latitudinal and temporal distributions of both frontal dust storms and lower atmosphere transient temperature anomalies show suppressed eddy activity around northern winter solstice. This is consistent with MGCM simulations of surface pressure [Hourdin et al., 1995]. Compared to the early/mid fall and mid/late winter periods, the boundary of the polar vortex during the winter solstice period exhibits a cone structure whose walls slope sharply towards the pole with altitude. Such a vortex shape is associated with a sharp temperature gradient and large static stability at the vortex edge. The polar vortex during the winter solstice period is smaller, more circular and stronger. Though the temporal baroclinic eddy growth rate (a theoretical value for unstable waves based on

linear theory) attains its maximum near northern winter solstice, the low-level transient eddy temperature amplitudes shows a minimum and no dust storm during this period exhibits classical frontal structure. Since the polar night area during the solstice period is the largest, it is hard to identify dust events near the terminator in this period and, since the CO_2 ice cap has its greatest southern extent, the regions of the strongest stresses associated with the wave likely lie over frosted surfaces, hence no dust lifting. Linear growth rates are likely irrelevant for traveling waves, which are of finite amplitude, and are largely equilibrated. Since the zonal wave number 2 and 3 topographic forcing decreases with latitude in the northern hemisphere, and topography plays key roles in localizing transient eddies, as the polar vortex shrinks towards the pole around northern winter solstice, the topographic effect on the polar circulation may get weaker, which is consistent with the absence of flushing storms during the solstice period.

The seasonal variability of traveling wave activity is brought out in Hourdin et al. [1995]. Collins et al. [1996] discuss the phenomena of zonal wave transitions in model studies. Leroy et al. [2003] shows the seasonal variability of simulated waves 1 and 2-3. The latter are most prominent in the L_s 180°-230° season. Simulations show that the strongest meridional velocities are associated with the higher wavenumbers, so it is not surprising that dust lifting events are associated with m=3 traveling waves. It is reasonable that topography could modulate the stresses associated with these waves. GCM simulations with parameterized dust lifting -[Basu et al. 2005, in preparation] do, in fact, show that m=3 traveling waves with 2-sol period are dominant in initiating the Chyrse-type storm that are prominent in their simulations in the L_s 210°-230° season. These waves particularly trigger lifting in the region of Alba Paterra, and dust is advected downstream, and, sometimes, into flushing storm events.

Acknowledgement

This research project is supported by NASA grant NRA-02-0SS-01. We thank John Wilson for detailed comments on improving the manuscript.

References

Albee, A. L., et al. (2001), Overview of the Mars Global Surveyor mission, *Journal Of Geophysical Research-Planets*, *106*, 23291-23316.

Banfield, D., et al. (2004), Traveling waves in the Martian atmosphere from MGS TES Nadir data, *Icarus*, *170*, 365-403.

Banfield, D., et al. (2003), Forced waves in the martian atmosphere from MGS TES nadir data, *Icarus*, *161*, 319-345.

Barnes, J. R. (1980), Time Spectral-Analysis Of Mid-Latitude Disturbances In The Martian Atmosphere, *Journal Of The Atmospheric Sciences*, *37*, 2002-2015.

Barnes, J. R. (1981), Mid-Latitude Disturbances In The Martian Atmosphere - A 2nd Mars Year, *Journal Of The Atmospheric Sciences*, *38*, 225-234.

Barnes, J. R. (1984), Linear Baroclinic Instability In The Martian Atmosphere, *Journal Of The Atmospheric Sciences, 41*, 1536-1550.

Barnes, J. R., et al. (1993), Mars Atmospheric Dynamics As Simulated By The Nasa Ames General-Circulation Model.2. Transient Baroclinic Eddies, *Journal Of Geophysical Research-Planets*, *98*, 3125-3148.

Basu, S., et al., in preparation, Simulation of spontaneous and variable global dust storms with the GFDL Mars GCM.

Cantor, B. A., et al. (2001), Martian dust storms: 1999 Mars Orbiter Camera observations, *Journal Of Geophysical Research-Planets*, *106*, 23653-23687.
Chang, E. K. M. (2001), GCM and observational diagnoses of the seasonal and interannual variations of the Pacific storm track during the cool season, *Journal Of The Atmospheric Sciences, 58*, 1784-1800.
Christensen, P. R., et al. (2001), Mars Global Surveyor Thermal Emission Spectrometer experiment: Investigation description and surface science results, *Journal Of Geophysical Research-Planets*, *106*, 23823-23871.
Collins, et al. (1996), Baroclinic wave transitions in the Martian atmosphere, *Icarus, 120*, 344-357.
Conrath, B. J., et al. (2000), Mars Global Surveyor Thermal Emission Spectrometer (TES) observations: Atmospheric temperatures during aerobraking and science phasing, *Journal Of Geophysical Research-Planets*, *105*, 9509-9519.
French, R. G., et al. (1981), Global patterns in cloud forms on Mars, *Icarus, 45*, 468-493.
Haberle, R. M., et al. (1993), Mars Atmospheric Dynamics As Simulated By The Nasa Ames General-Circulation Model.1. The Zonal-Mean Circulation, *Journal Of Geophysical Research-Planets*, *98*, 3093-3123.
Harnik, N., and E. K. M. Chang (2004), The effects of variations in jet width on the growth of baroclinic waves: Implications for midwinter Pacific storm track variability, *Journal Of The Atmospheric Sciences*, *61*, 23-40.
Hinson, D. P. and R. J. Wilson (2002), Transient eddies in the southern hemisphere of Mars, *GRL, 29*, Art. No. 1154.
Hinson, D. P., et al. (2004), Comparison of atmospheric temperatures obtained through infrared sounding and radio occultation by Mars Global Surveyor, *Journal Of Geophysical Research-Planets, 109*, Art. No. E12002.
Hollingsworth, J. L., et al. (1996), Orographic control of storm zones on Mars, *Nature*, *380*, 413-416.
Hollingsworth, J. L., et al. (1997), Seasonal variations of storm zones on Mars, in *Planetary Atmospheres And Ionospheres And Reference Atmospheres*, edited, pp. 1237-1240.
Holton, J. R., (1992), An introduction to dynamic meteorology, 511pp, Academic Press, San Diego.
Hourdin, F., et al. (1995), The sensitivity of the Martian surface pressure and atmospheric mass budget to various parameters - A comparison between numerical simulations and Viking observations, *Journal of Geophysical Research-Planets, 100*, 5501-5523.
James, P. B., et al. (1999), North polar dust storms in early spring on Mars, *Icarus*, *138*, 64-73.
Kahn, R., (1984), The spatial and seasonal distribution of Martian clouds and some meterological implications, *Journal Of Geophysical Research-Planets, 89*, 6671-6688.
Leroy, S. S., et al. (2003), Principal modes of variability of Martian atmospheric surface pressure, *GRL, 30*, Art. No. 1707.
Malin, M. C., and K. S. Edgett (2001), Mars Global Surveyor Mars Orbiter Camera: Interplanetary cruise through primary mission, *Journal Of Geophysical Research-Planets*, *106*, 23429-23570.
Nakamura, H. (1992), Midwinter Suppression Of Baroclinic Wave Activity In The Pacific, *Journal Of The Atmospheric Sciences*, *49*, 1629-1642.

Newman, C. E., et al. (2002), Modeling the Martian dust cycle - 2. Multiannual radiatively active dust transport simulations, *Journal Of Geophysical Research-Planets, 107,* Art. No. 5124.
Neumann, G. A., et al. (2003), Two Mars years of clouds detected by the Mars Orbiter Laser Altimeter, *Journal Of Geophysical Research-Planets, 108*, Art. No. 5023.
Smith, M. D., et al. (2002), Thermal Emission Spectrometer observations of Martian planet-encircling dust storm 2001A, *Icarus*, *157*, 259-263.
Smith, M. D. (2004), Interannual variability in TES atmospheric observations of Mars during 1999-2003, *Icarus, 167*, 148-165.
Strausberg, M. J., et al. (2005), Observations of the Initiation and evolution of the 2001 Mars Global Dust Storm, *Journal of Geophysical Research-Planets,* in press.
Wang, H. Q., and A. P. Ingersoll (2002), Martian clouds observed by Mars Global Surveyor Mars Orbiter Camera, *Journal Of Geophysical Research-Planets*, *107*.
Wang, H. Q., et al. (2003), Cyclones, tides, and the origin of a cross-equatorial dust storm on Mars, *Geophysical Research Letters*, *30*.
Wilson, R. J., et al. (2002), Traveling waves in the Northern Hemisphere of Mars, *Geophysical Research Letters*, *29*.
Zurek, R. W., et al. (1992), Dynamics of the atmosphere of Mars, in Mars, Ed. Kieffer, H. H., B. M. Jakosky, C. W. Snyder, and M. S. Matthews, Univ. of Arizona Press, 835-933.

Tables

	$X<-\sigma$	$-\sigma<X<\sigma$	$X>\sigma$	$X<-2\sigma$	$-2\sigma<X<2\sigma$	$X>2\sigma$
ΔT	52%	47%	16%	9%	89%	2%
Gaussian	16%	68%	16%	2.3%	95.4%	2.3%

Table 1. Proportion of data within different probability sectors (Figure 7) for the actual distribution of observed extreme temperature anomalies and for comparison the Gaussian (random) distribution. That many more than 16% of observations are at greater negative values suggests a statistically significant correlation of negative temperatures with the trailing air mass of observed fronts.

Figure Captions

Figure 1. A variety of polar stereographically projected daily global maps encountered during storm identification. Fig. 1d, e cover the whole northern hemisphere, while the others cover the area north of 45ºN. Identified frontal storms are indicated by arrows pointing to their ID numbers at the southern edges of the events in the images. Fig. 1a, e show examples of small fronts scattered around the polar cap. Their morphologies range from linear dust band extending southward from

the polar cap (Fig. 1e) to various kinds of curved bands around the cap edge (Fig. 1a). Fig. 1b, c and d show large storms possessing classical frontal features characteristic of terrestrial baroclinic storms. The feature indicated by the question mark in Fig. 1c appears as a streak that extends more than half a circumstance around the pole. It is possibly formed by stretching a former front by strong winds. Such long streaky features do not count in the catalog. The question marks in Fig. 1d and e refer to the numerous thin streaks that appear to be circling around or spiraling into the pole. These streaks in the polar hood are not included in the catalog, neither. The L_s values are (a) 162°, (b) 184°, (c) 188°, (d) 221°, (e) 242° and (f) 357°.

Figure 2. The plotted data points correspond to the southern edges of dust fronts that were listed as new dust events in the catalog. The spatial distribution data show that most of the frontal dust storms were concentrated in the low topographic regions of Acidalia, Arcadia and Utopia. The middle panel shows the latitudinal and seasonal distribution of frontal dust storms from late northern summer (L_s=150º) to the northern summer solstice of the next Martian year (L_s=90º). Periods with missing data are indicated in the figure. The curve corresponds to the edge of polar night (terminator). The lower panel of Fig. 2 is a histogram showing the number of storms within each 10º-degree L_s bin as a function of L_s.

Figure 3. Spatial and temporal distributions of frontal dust storms in MGS Year 2. The upper panel shows the latitude – (west) longitude distribution of the southern edges of the storms. The middles panel shows the latitude – L_s distribution of the southern edges of the storms. The curve corresponds to the edge of polar night. The lower panel is a histogram showing the number of frontal dust storms in 10° L_s bin as a function of L_s. Data gaps and northern winter solstice (L_s = 270°) are annotated and indicated by arrows. The time period for the Hellas global dust storm is indicated by the thick line under the horizontal axis of the middle panel.

Figure 4. Distribution in latitude and seasonal date (L_s) plot of the southern tips of frontal dust storms observed in MOC images to transport dust southward. Blue dots are for MGS mapping Year 1 (1999-2001), green for Year 2 (2001-2003), and red for Year 3 (2003-2005). The currently analyzed data last until L_s 270º in Year 3. Figure 4 does not include storms that only travel around the polar region but do not transport dust southward. Multi-day events gets multiple dots in Fig. 4, with one dot for each day, while in Fig. 2 and 3, multi-day events only get one dot corresponding to the first day.

Figure 5. Examples of flushing dust storms in different channels, seasons and years. Each panel is a Mars daily global map projected onto a sphere with black arrows pointing to the main frontal features. The three rows from the top to the bottom are for MGS Year 1, 2, and 3 respectively. (a), (b), (d), (e), (h) and (i) are for the Acidalia channel. (c) is for the Arcadia channel. (f) and (g) are for the Utopia channel. The L_s values are (a) 210°, (b) 314°, (c) 336°, (d) 316°, (e) 324°, (f) 324°, (g) 207°, (h) 214° and (i) 230°.

Figure 6. Temperature anomalies at 4.75 mb along TES tracks for the daily global maps (0° – 90°N) at L_s ~210° in MGS Year 1. East longitudes are shown along 45N,

and north latitudes are shown along 0 longitude. The numbers 0 – 12 next to the tracks are track IDs for this map.

Figure 7. Temperature anomalies associated with frontal dust storms at 6.1 mb. The horizontal axis is temperature anomaly. The vertical axis is the standard deviation of the temperature anomaly. The lines correspond to ±σ and ±2σ.

Figure 8. Standard deviations of daytime transient temperature perturbations as a function of latitude and Ls. The top row is for 4.75 mb, and the bottom row for 2.24 mb. The columns from left to right correspond to MGS Year 1, 2, and 3 respectively.

Figure 9. Parameters derived from the zonal mean TES temperature data. The left column is for 4.75 mb (i.e. a log-pressure height of 2.5 km). The right column is for 2.24 mb (10 km). Diamonds are for MGS Year 1, stars for Year 2, and squares for Year 3. The horizontal axis for each panel is Ls. The first row from the top is the latitude of the edge of polar vortex defined as the latitude that corresponds to the minimum $\frac{dT}{dy}$. The second row is the $\frac{dT}{dy}$ at the vortex edge. The third row is the static stability squared (N^{*2}) at the vortex edge. The fourth row is the baroclinic parameter (α) which is proportional to the growth rate of the most unstable Eady mode.

Figure 10. Latitude – longitude distribution of standard deviations of transient temperature perturbations for selected 30° L_s periods in MGS Year 1. The L_s periods for the panels are (a) 160° – 190°, (b) 200° – 230°, (c) 230° – 260°, (d) 270° – 300°, (e) 300° – 330° and (f) 330° – 360°.

Figure 11. Latitude – longitude distribution of standard deviations of transient temperature perturbations for selected 30° L_s periods in MGS Year 2. The L_s periods for the panels are (a) 160° – 190°, (b) 190° – 220°, (c) 240° – 270°, (d) 270° – 300°, (e) 310° – 340° and (f) 330° – 360°.

Figure 12. Power of eastward traveling waves with periods between 2 and 8 sols. Each panel is a latitude – L_s plot. The top row is for 4.75 mb. The bottom row is for 2.24 mb. The three columns from the left to the right are for zonal wave number m = 1, 2 and 3 respectively.

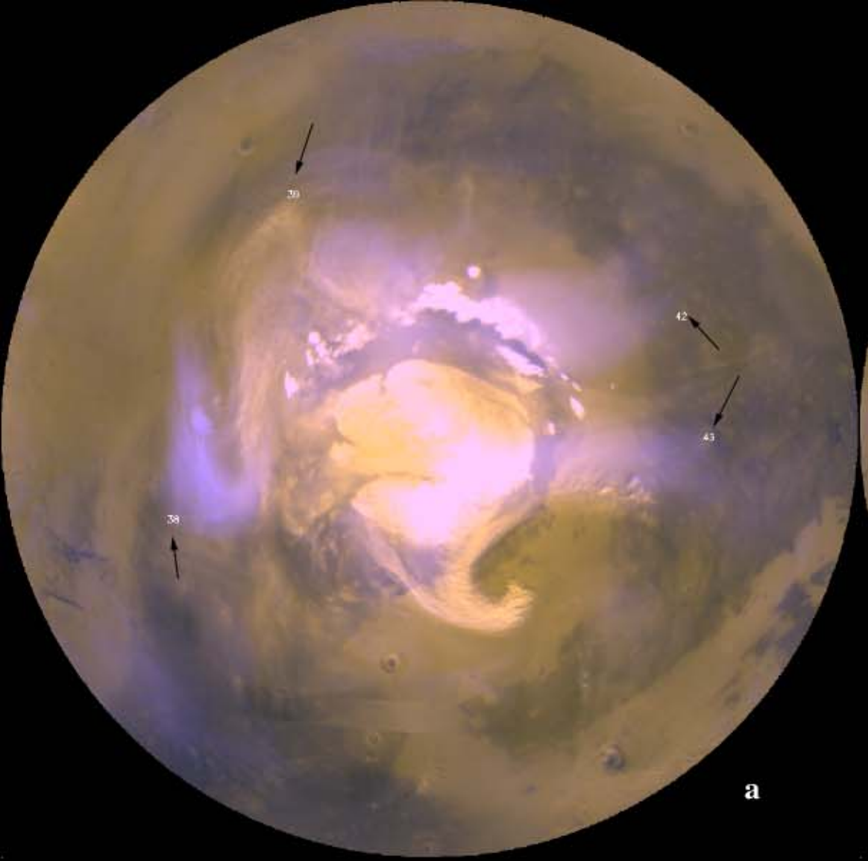

a

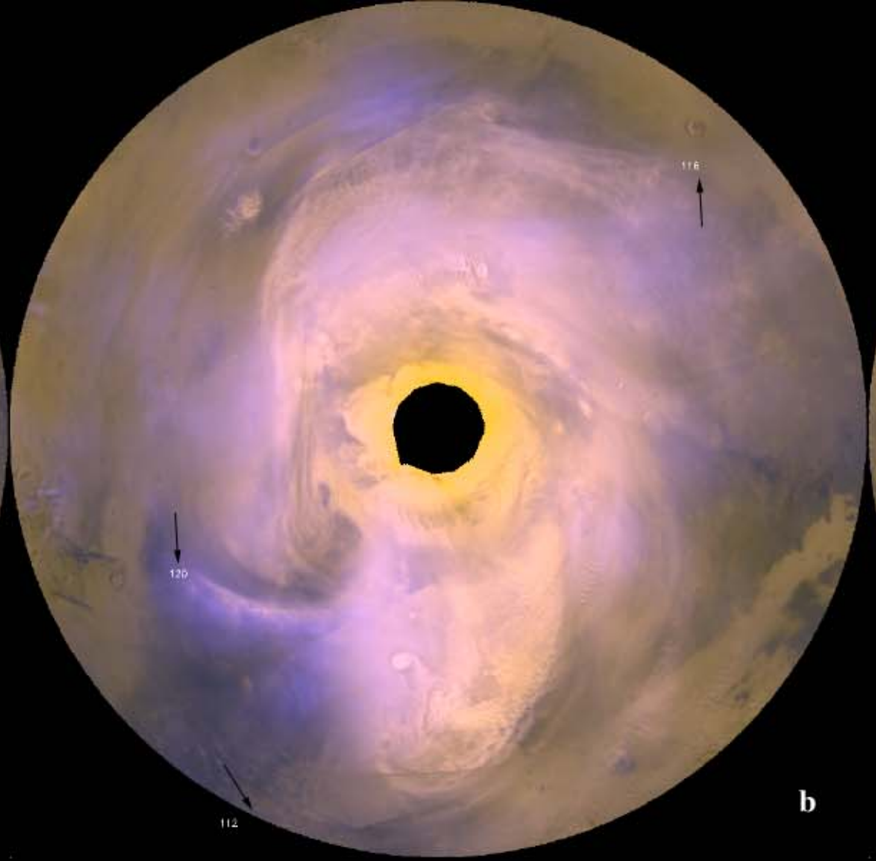

b

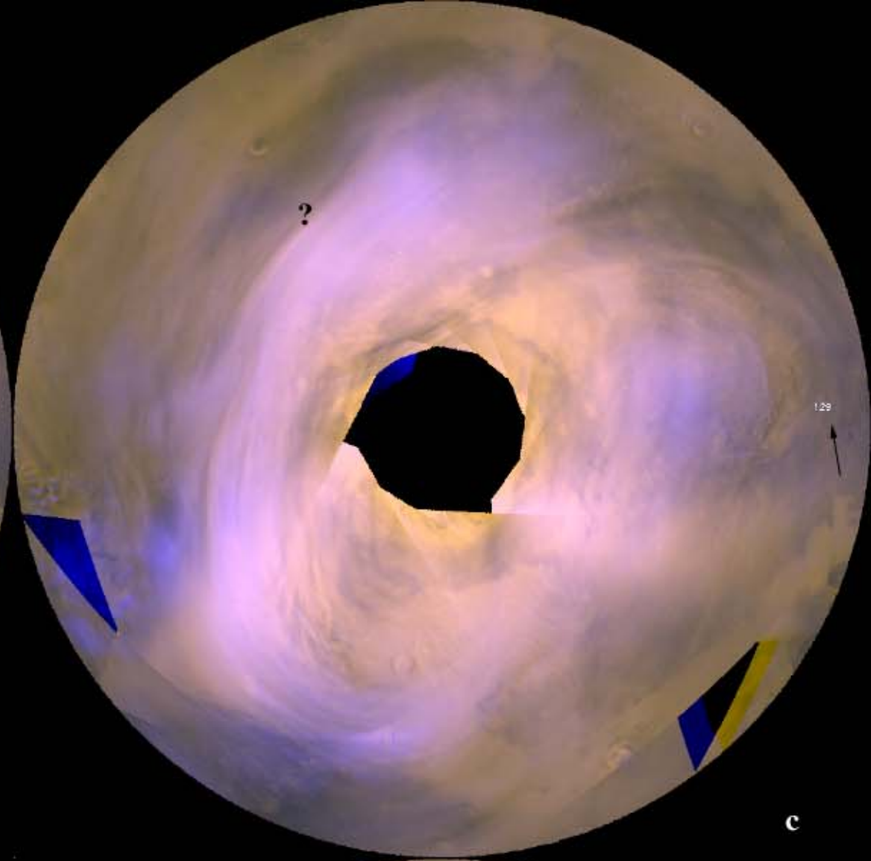

c

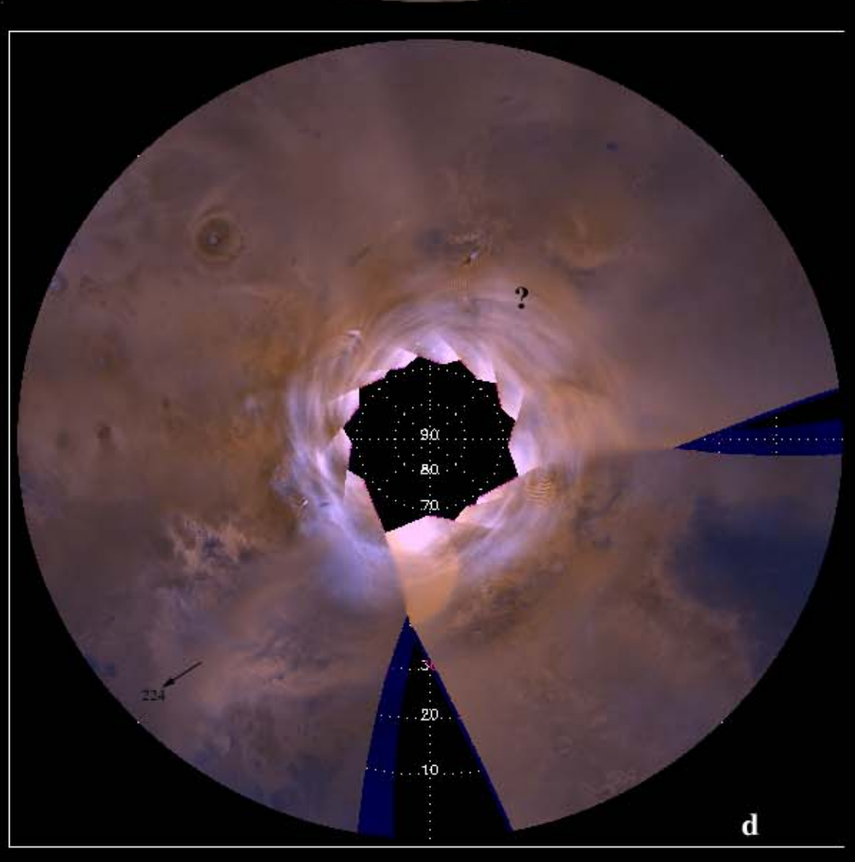

d

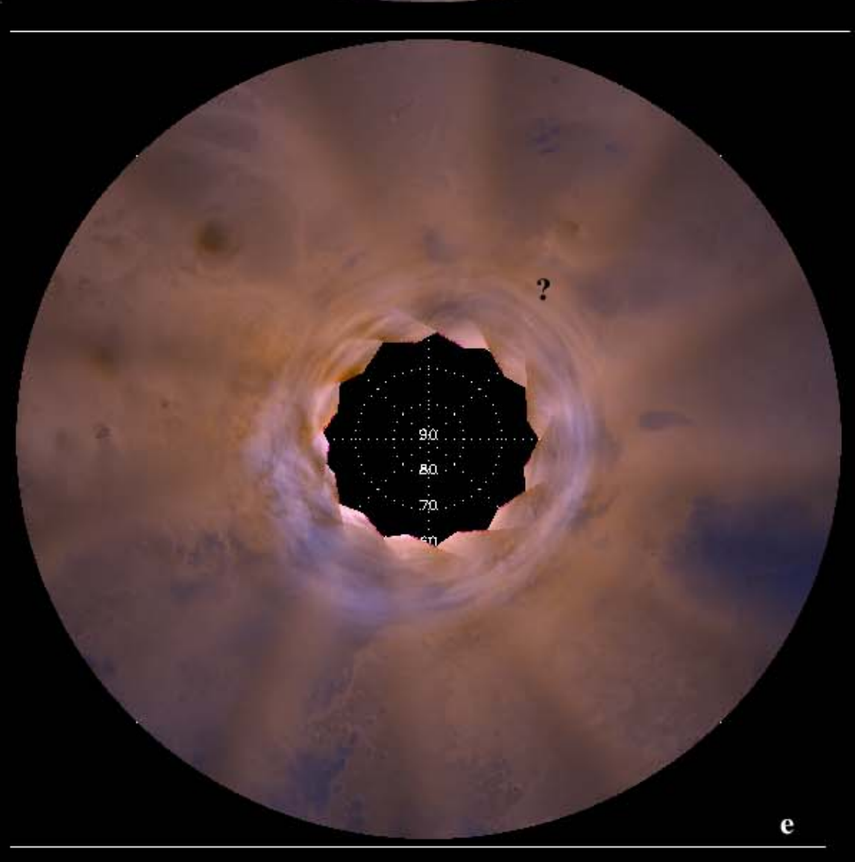

e

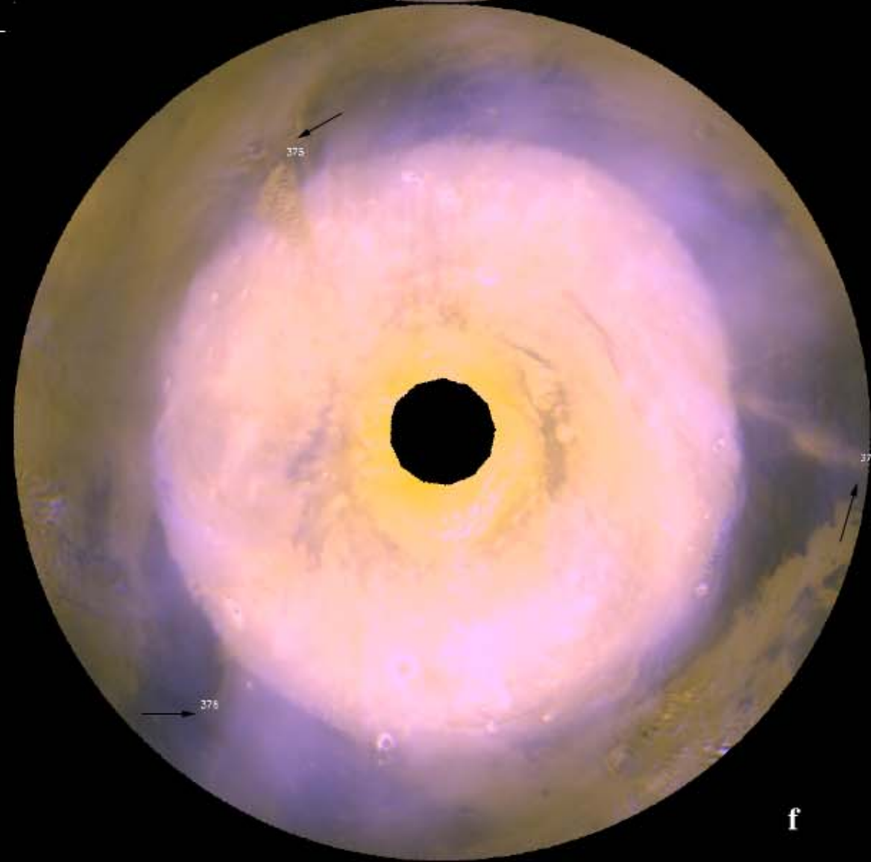

f

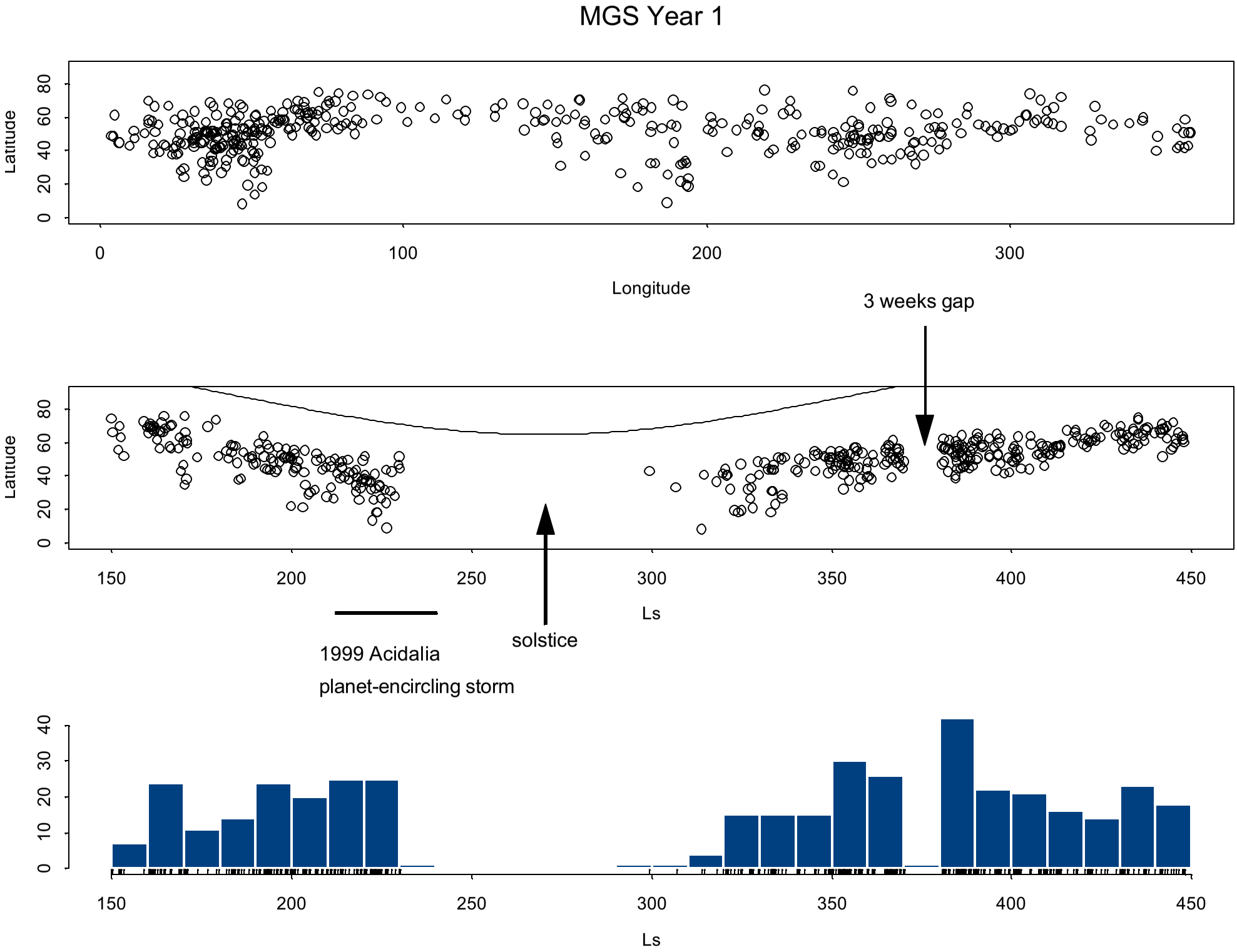
MGS Year 1
Latitude
0
20
40
60
80
0
100
200
300
Longitude
3 weeks gap
Latitude
0
20
40
60
80
150
200
250
300
350
400
450
Ls
solstice
1999 Acidalia
planet-encircling storm
0
10
20
30
40
150
200
250
300
350
400
450
Ls

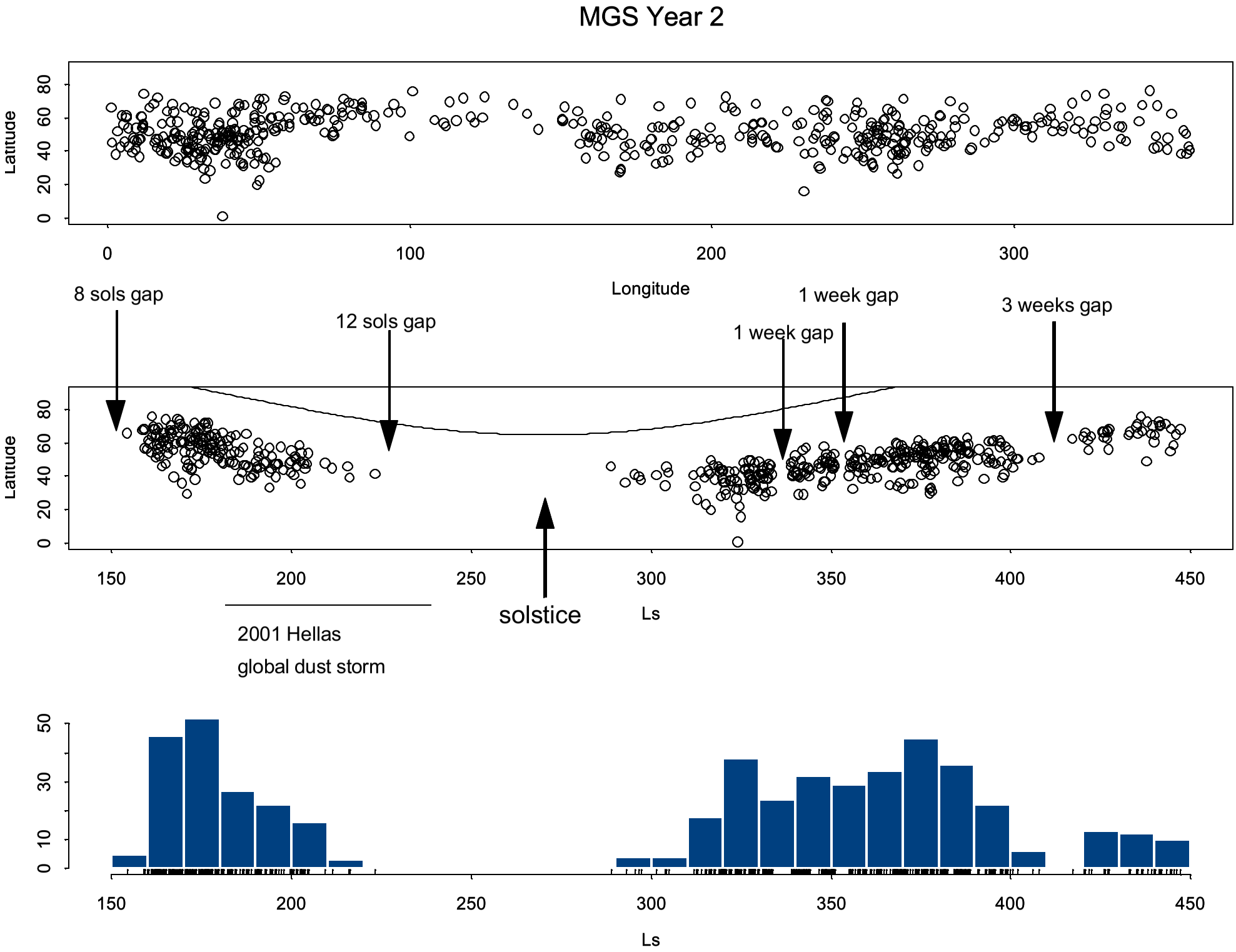
MGS Year 2
Latitude
0
20
40
60
80
0
100
200
300
Longitude
8 sols gap
12 sols gap
1 week gap
1 week gap
3 weeks gap
Latitude
0
20
40
60
80
150
200
250
300
350
400
450
solstice
Ls
2001 Hellas
global dust storm
0
10
30
50
150
200
250
300
350
400
450
Ls

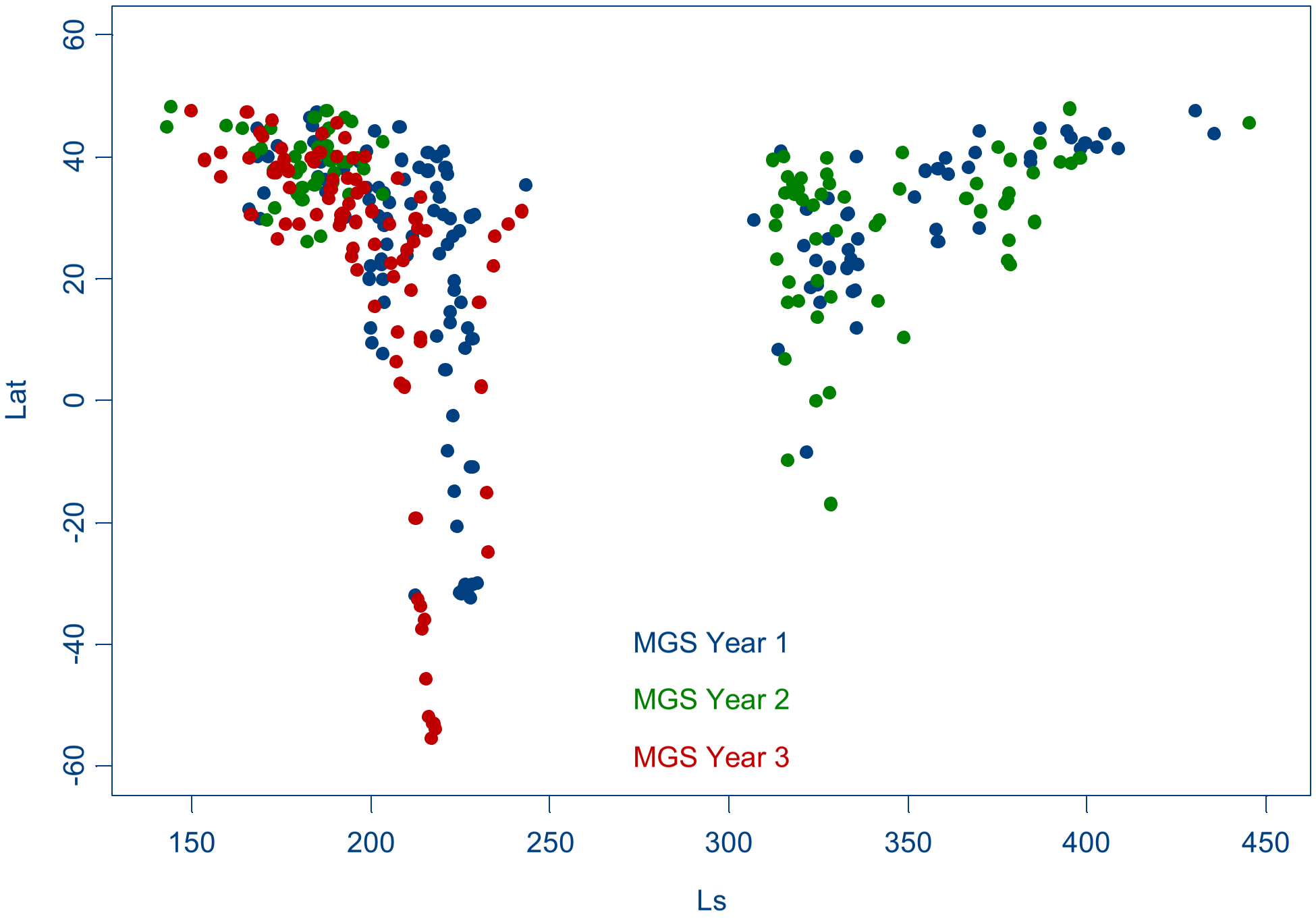
Lat
60
40
20
0
-20
-40
-60
150
200
250
300
350
400
450
Ls
MGS Year 1
MGS Year 2
MGS Year 3

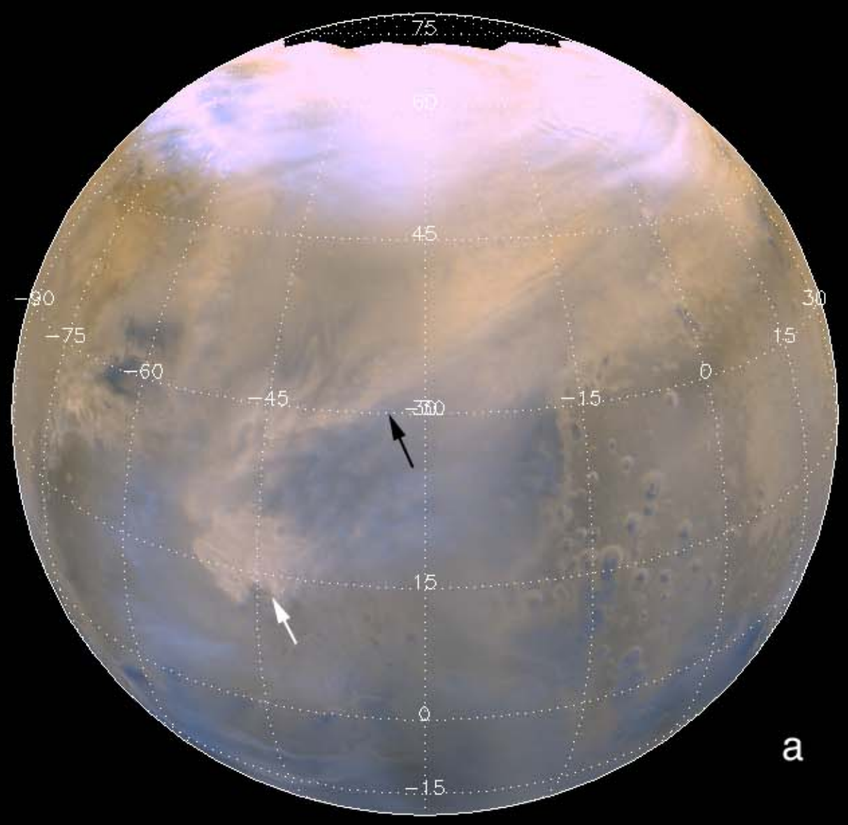
75
60
45
30
15
0
−15
−30
−45
−60
−75
−90

a


75
60
45
30
15
0
−15
−30
−45
−60
−75
−90

b

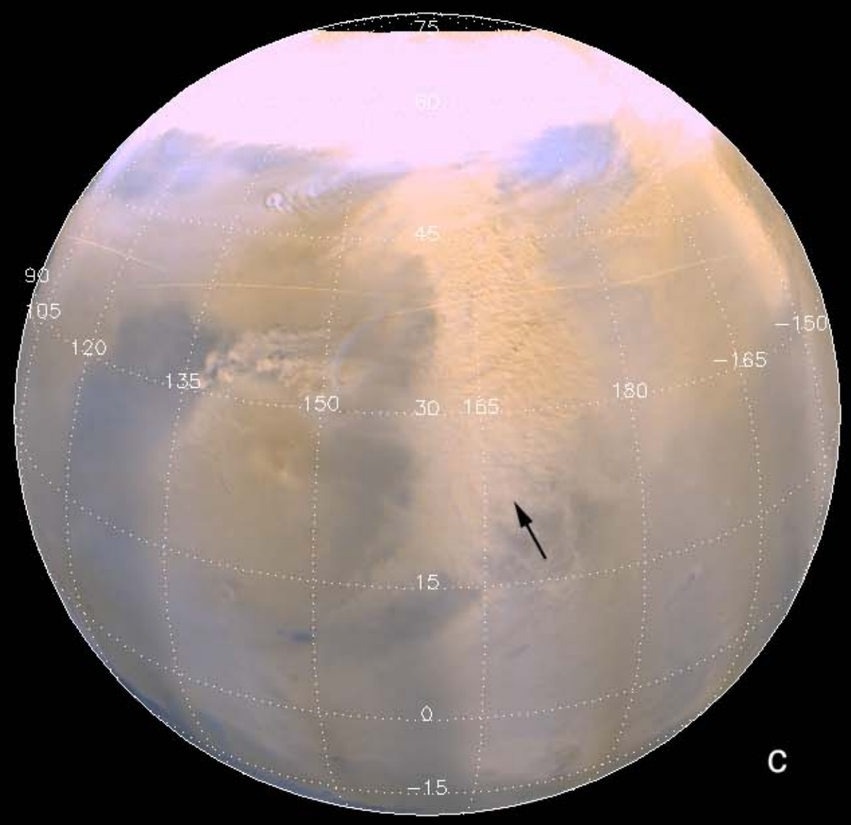
75
60
45
30
15
0
−15
−30
−45
−150
−165
180
165
150
135
120
105
90

c

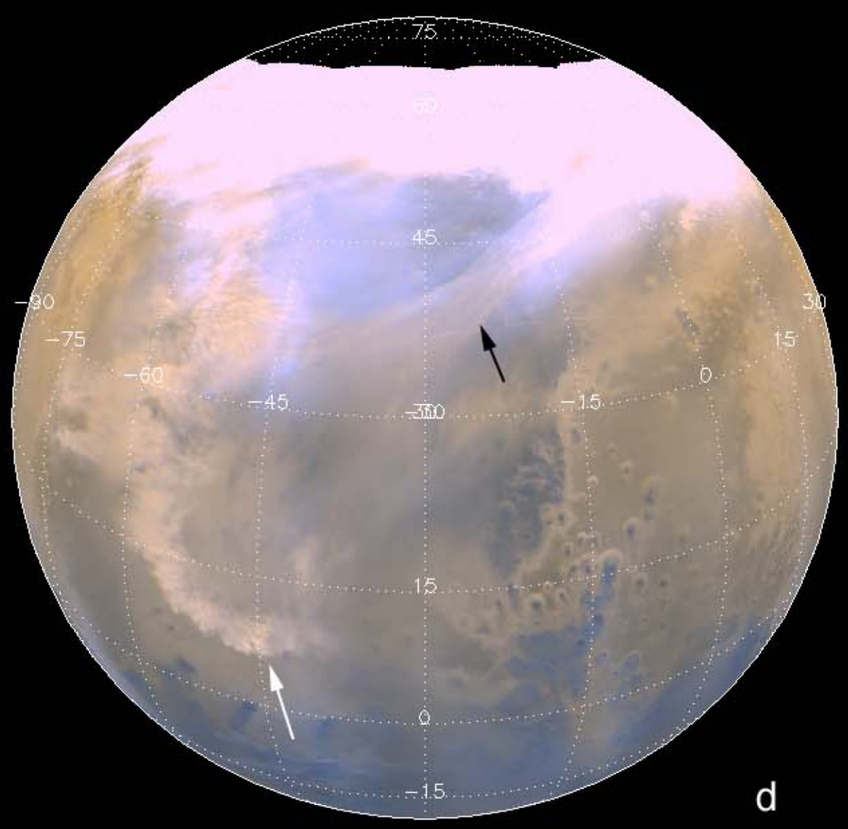
75
60
45
30
15
0
−15
−30
−45
−60
−75
−90

d

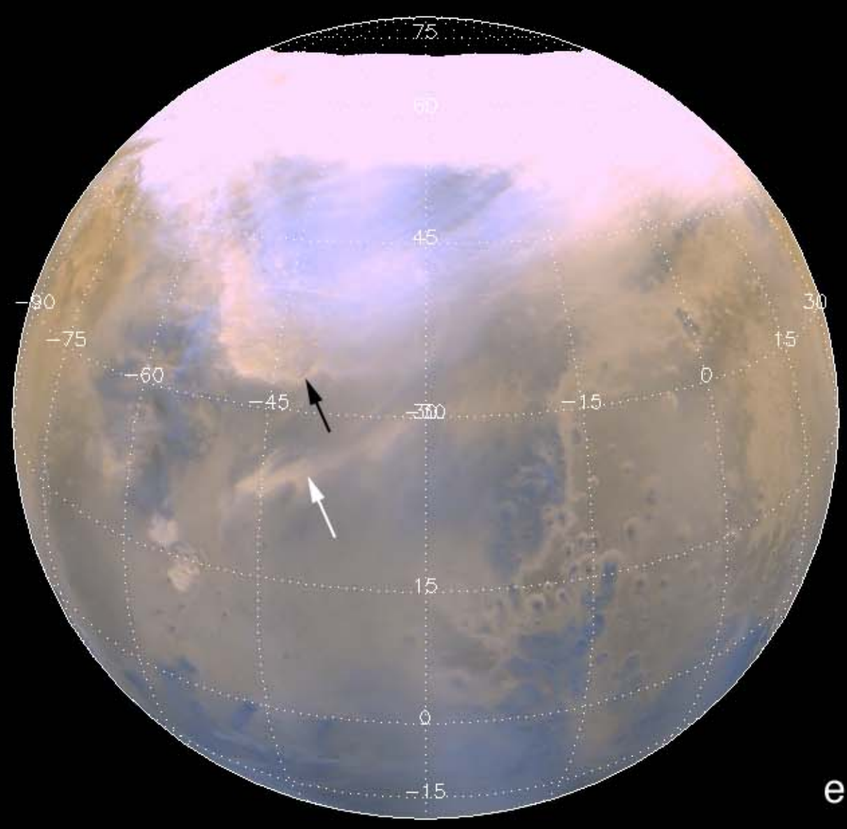
75
60
45
30
15
0
−15
−30
−45
−60
−75
−90

e

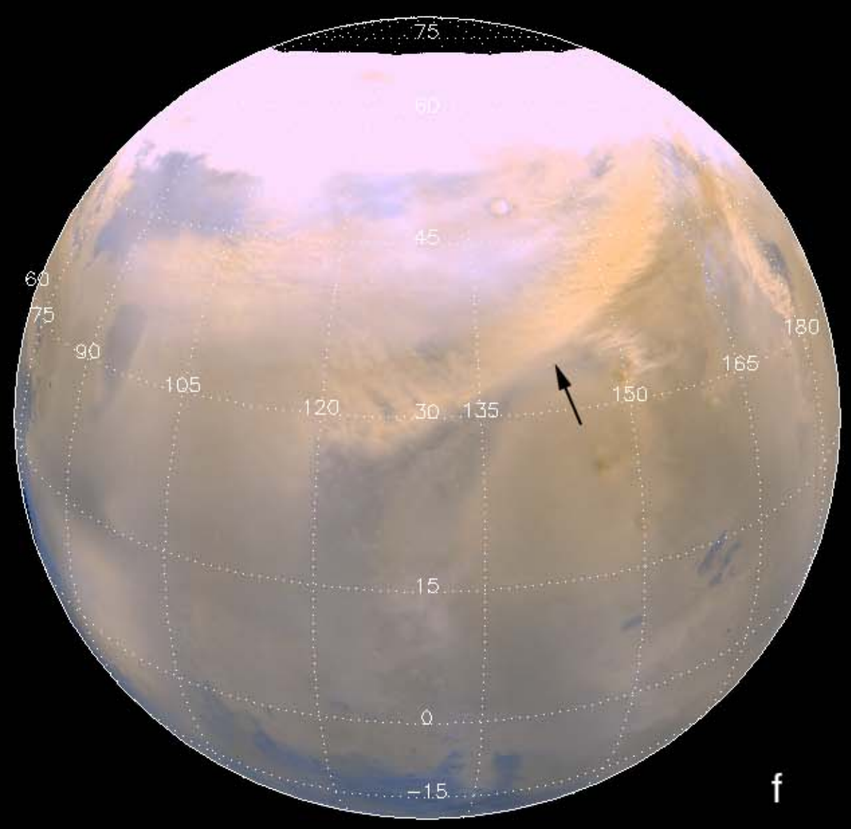
75
60
45
30
15
0
−15
−30
180
165
150
135
120
105
90
75
60

f

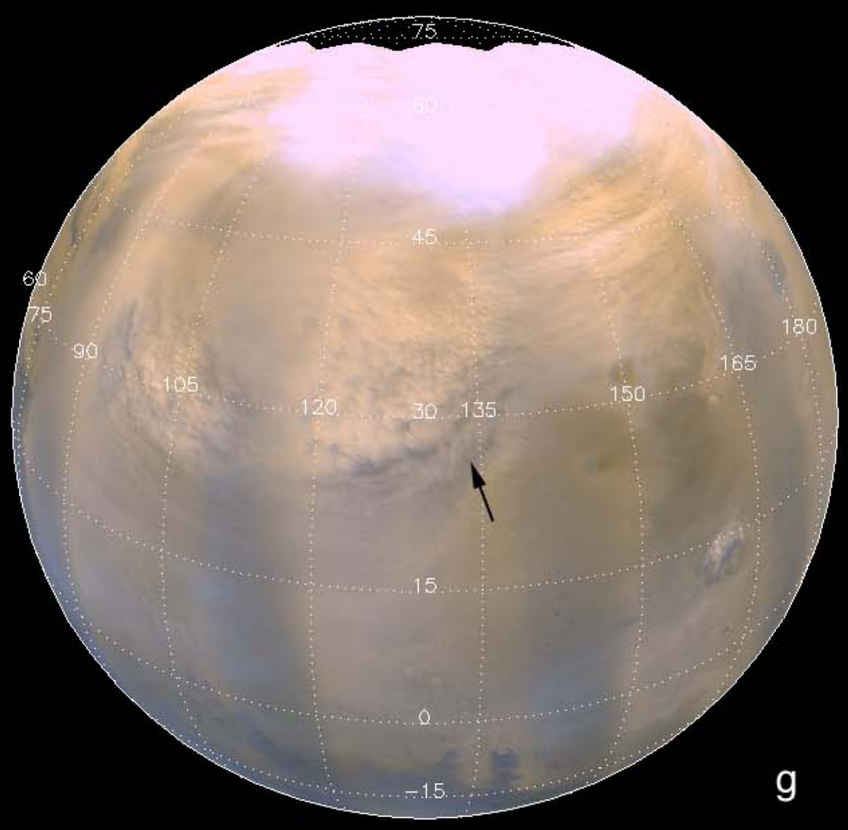
75
60
45
30
15
0
−15
−30
180
165
150
135
120
105
90
75
60

g

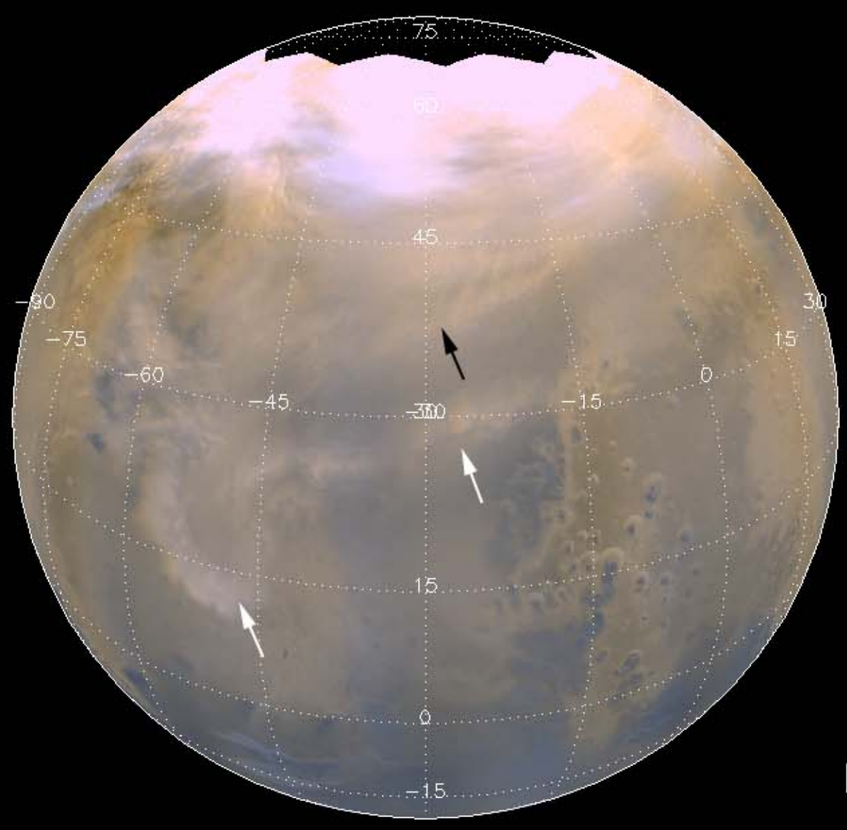
75
60
45
30
15
0
−15
−30
−45
−60
−75
−90

h


75
60
45
30
15
0
−15
−30
−45
−60
−75
−90

i

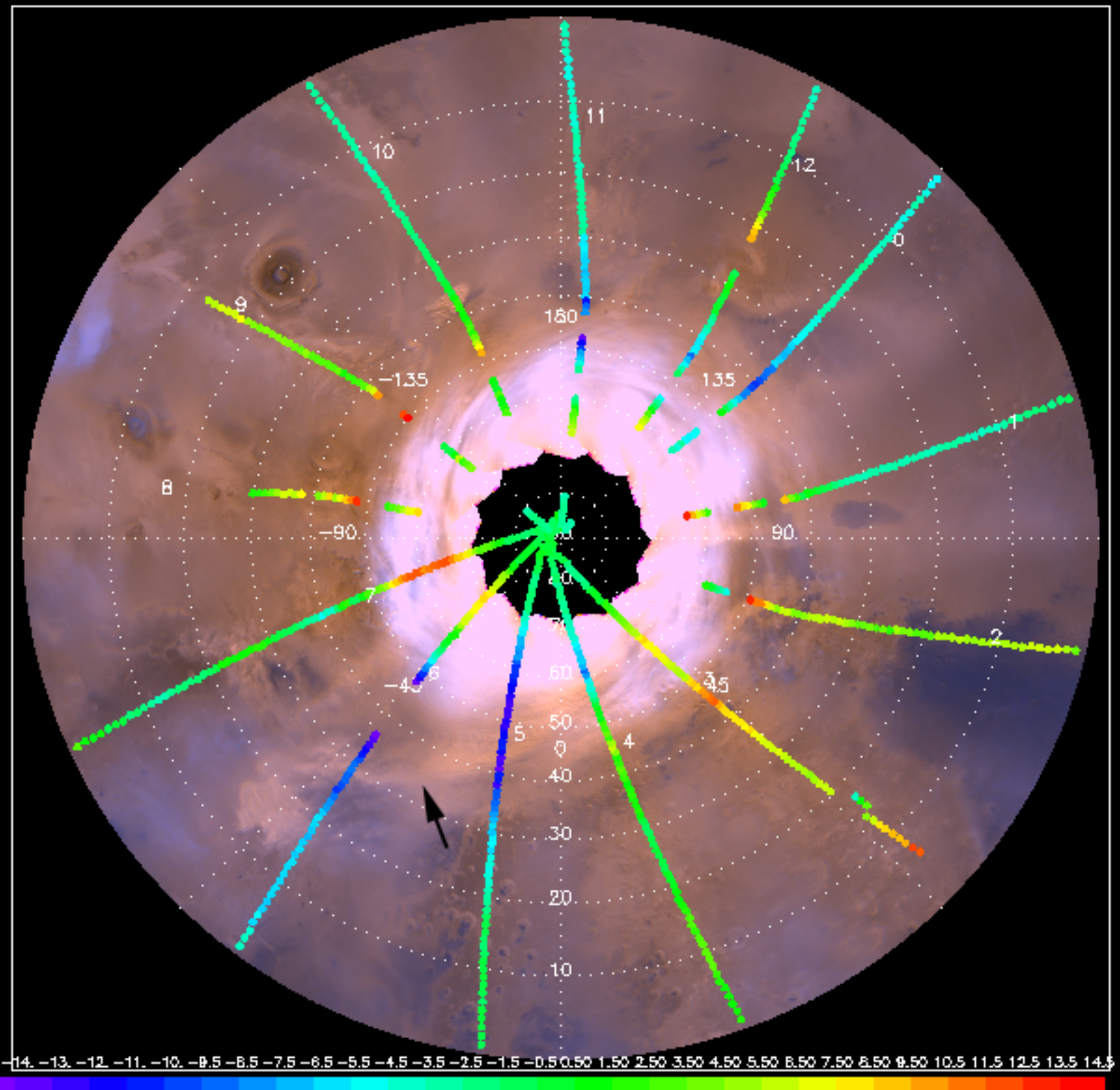
11
10
12
9
180
0
−135
135
8
1
−90
90
7
2
−45
45
6
5
4
3
50
40
30
20
10
−14. −13. −12. −11. −10. −9.5 −8.5 −7.5 −6.5 −5.5 −4.5 −3.5 −2.5 −1.5 −0.5 0.50 1.50 2.50 3.50 4.50 5.50 6.50 7.50 8.50 9.50 10.5 11.5 12.5 13.5 14.5

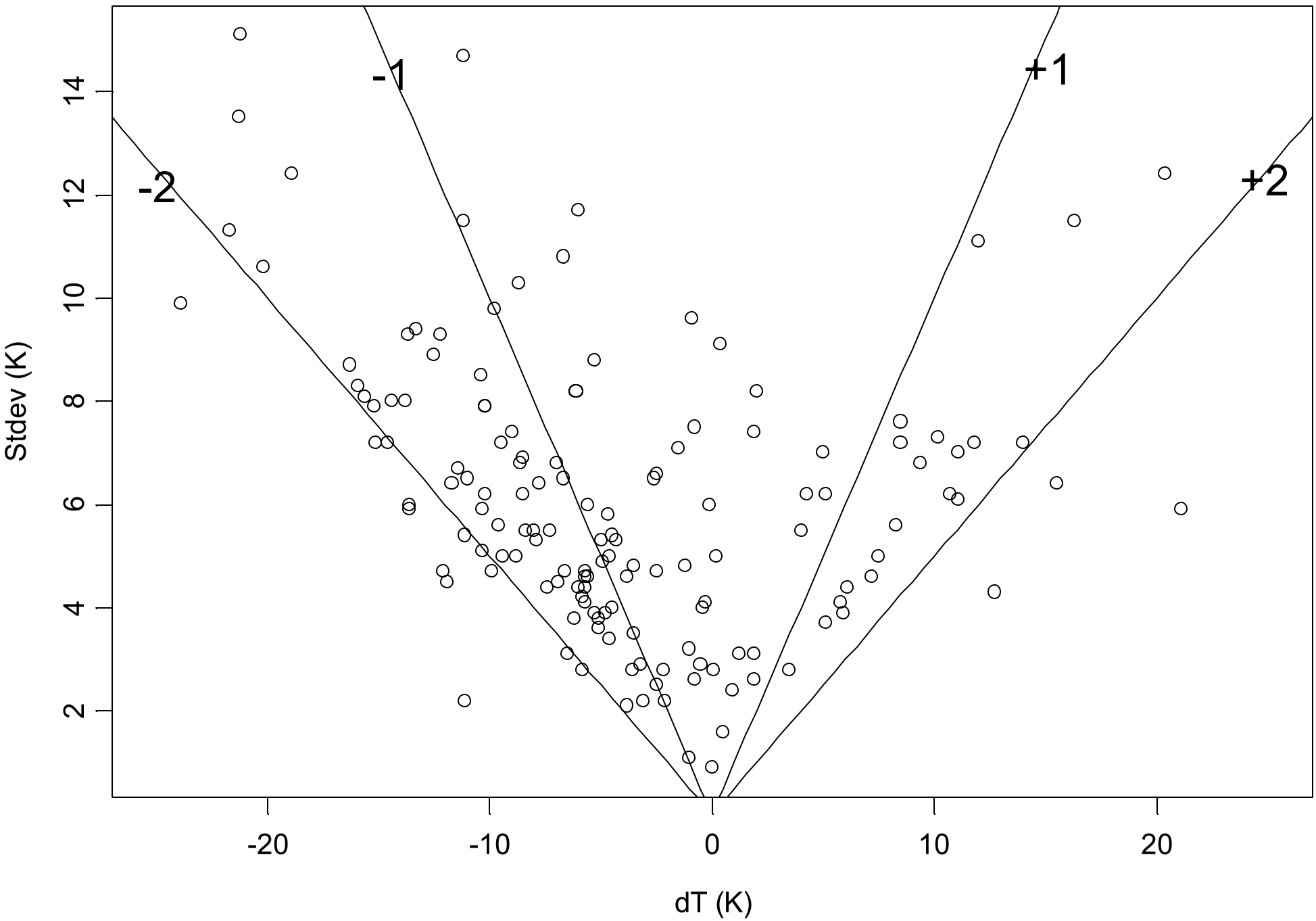
-2
-1
+1
+2
Stdev (K)
2
4
6
8
10
12
14
-20
-10
0
10
20
dT (K)

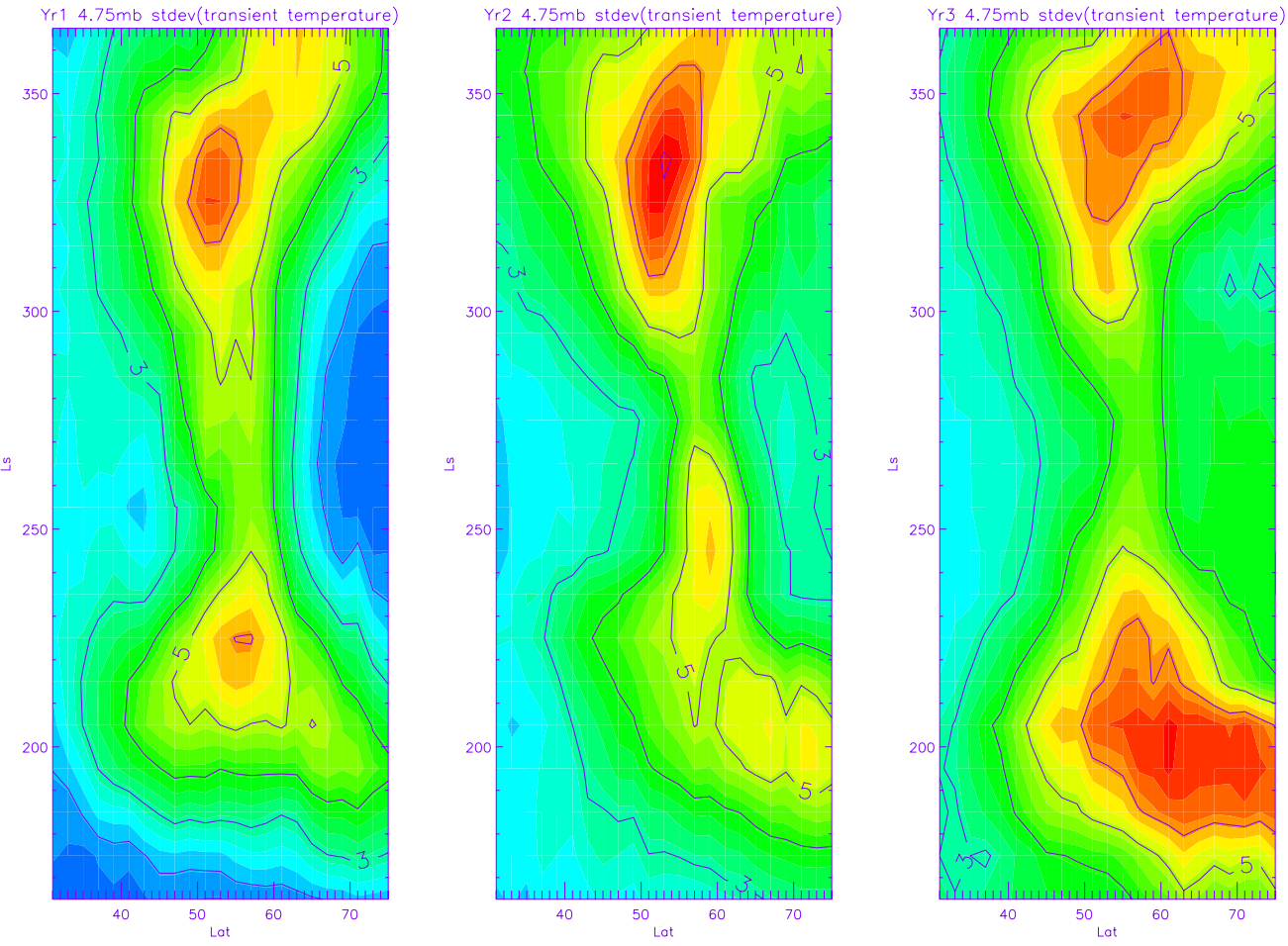
Yr1 4.75mb stdev(transient temperature)
Yr2 4.75mb stdev(transient temperature)
Yr3 4.75mb stdev(transient temperature)
Ls
Lat
350
300
250
200
40
50
60
70

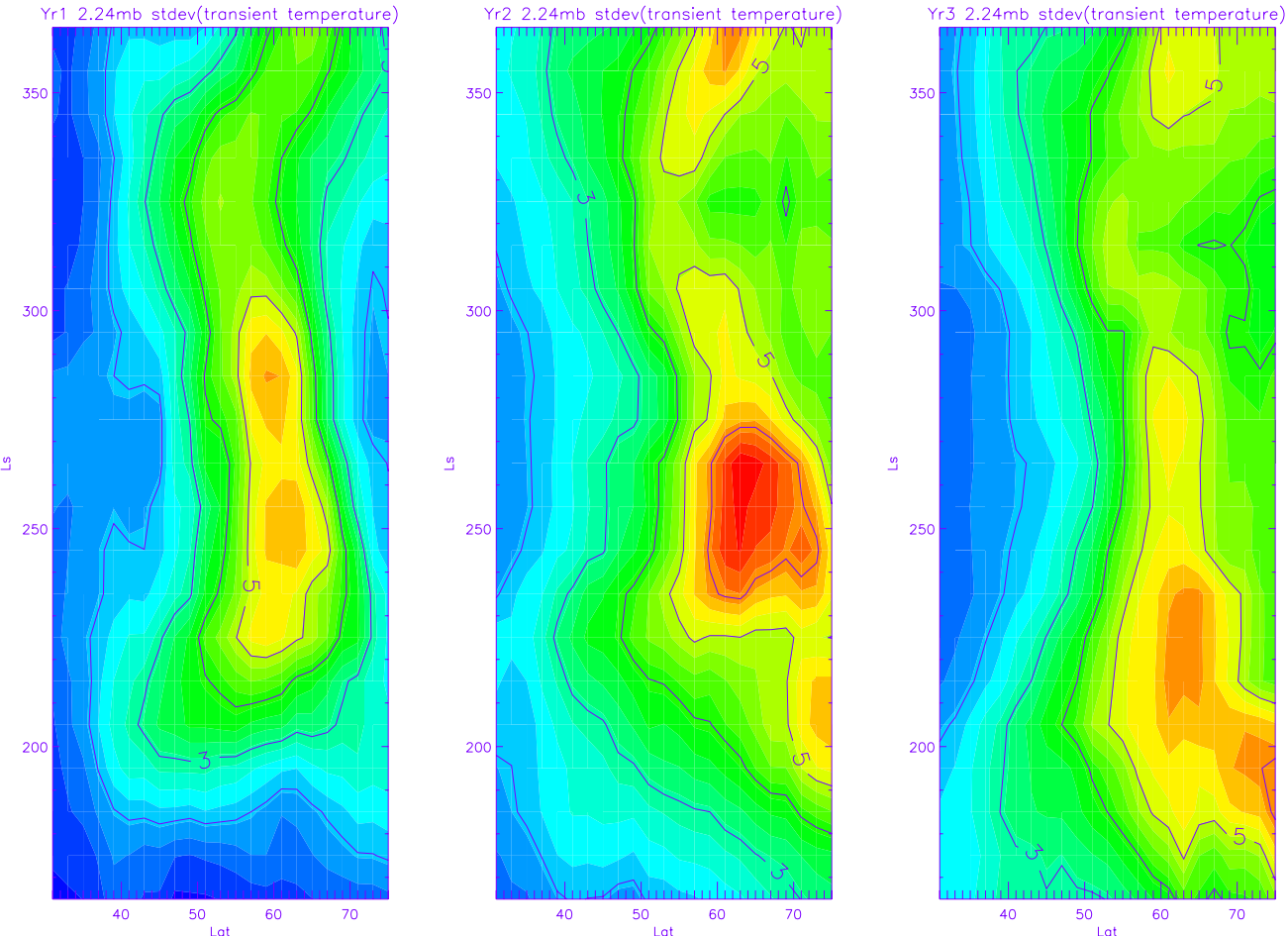
Yr1 2.24mb stdev(transient temperature)
Yr2 2.24mb stdev(transient temperature)
Yr3 2.24mb stdev(transient temperature)
Ls
Lat
350
300
250
200
40
50
60
70

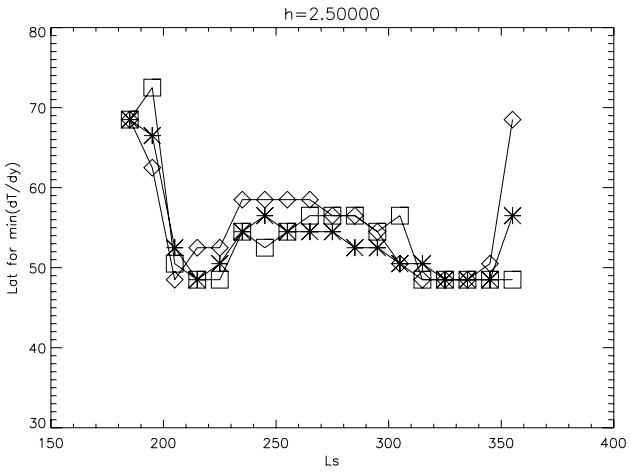
h=2.50000
Lat for min(dT/dy)
Ls

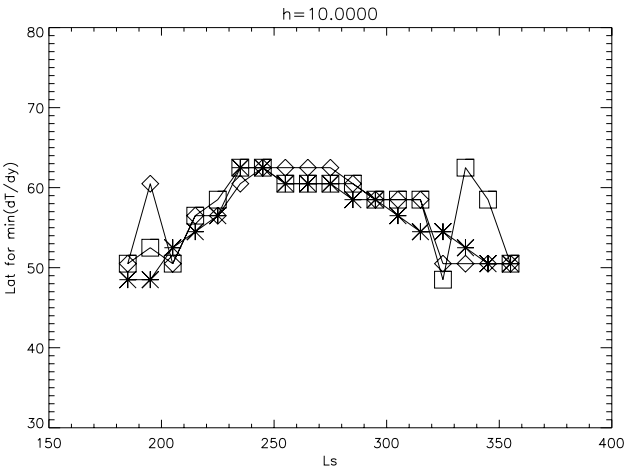
h=10.0000
Lat for min(dT/dy)
Ls

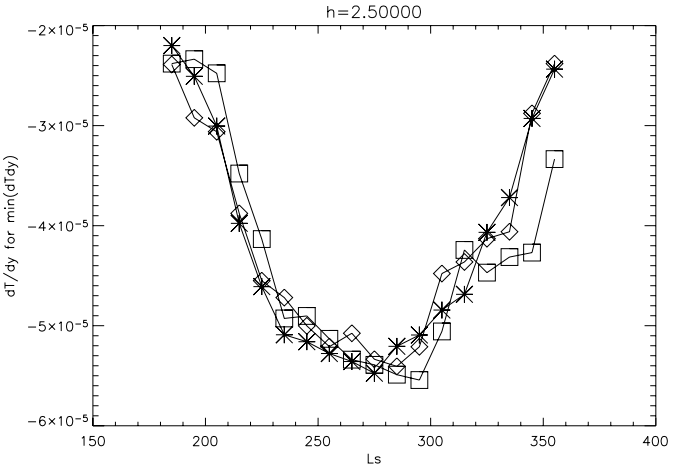
h=2.50000
dT/dy for min(dTdy)
Ls

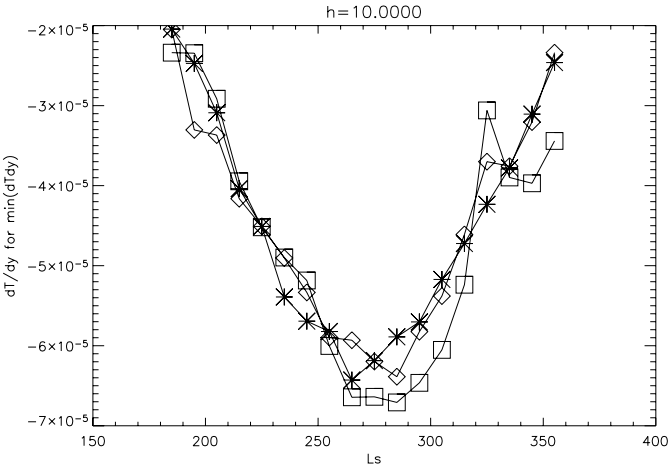
h=10.0000
dT/dy for min(dTdy)
Ls

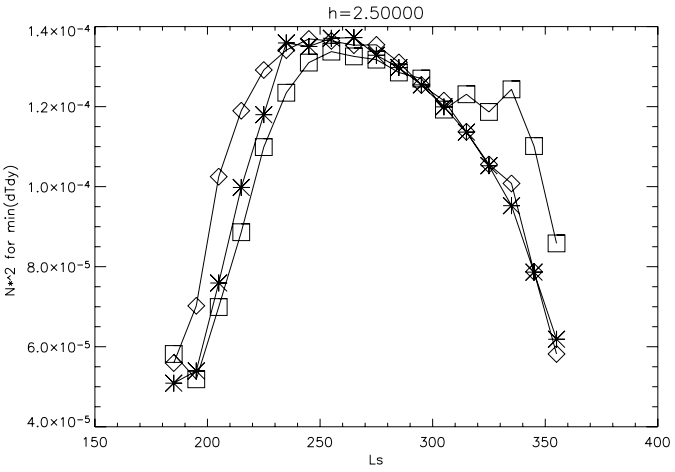
h=2.50000
N**2 for min(dTdy)
Ls

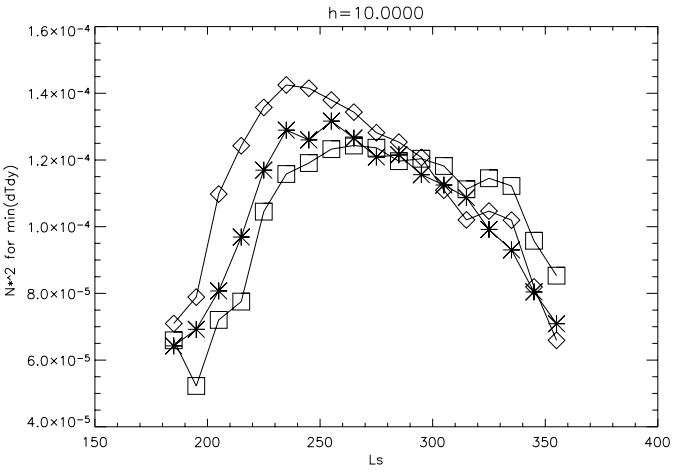
h=10.0000
N**2 for min(dTdy)
Ls

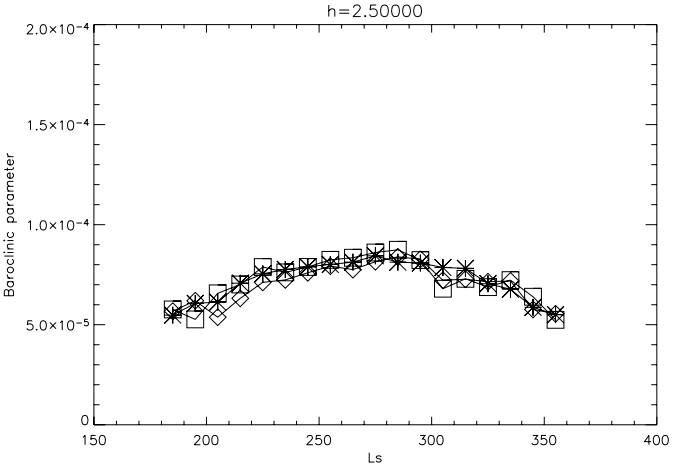
h=2.50000
Baroclinic parameter
Ls

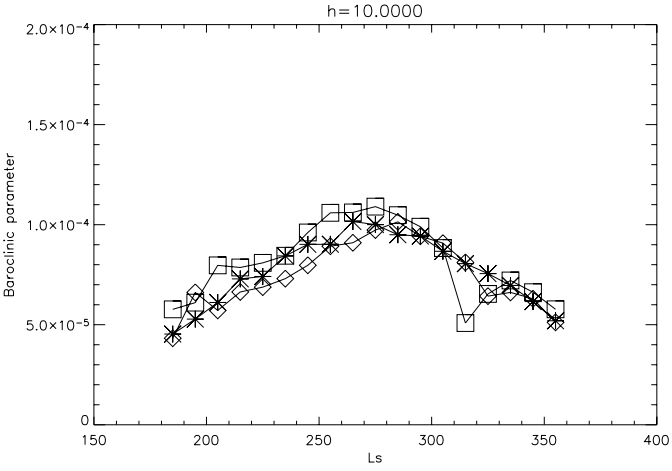
h=10.0000
Baroclinic parameter
Ls

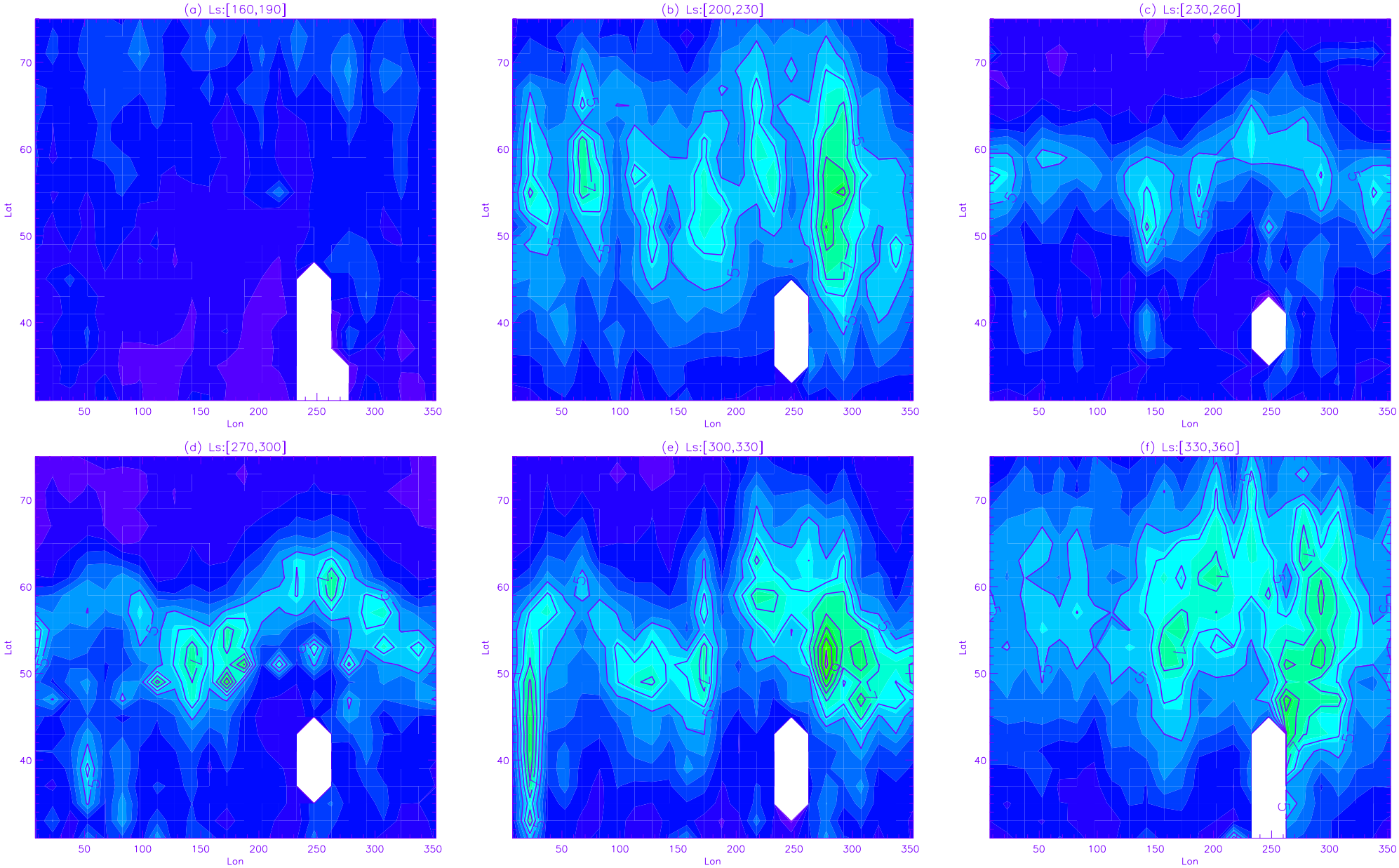
(a) Ls:[160,190]
(b) Ls:[200,230]
(c) Ls:[230,260]
(d) Ls:[270,300]
(e) Ls:[300,330]
(f) Ls:[330,360]
Lat
Lon
70
60
50
40
50
100
150
200
250
300
350

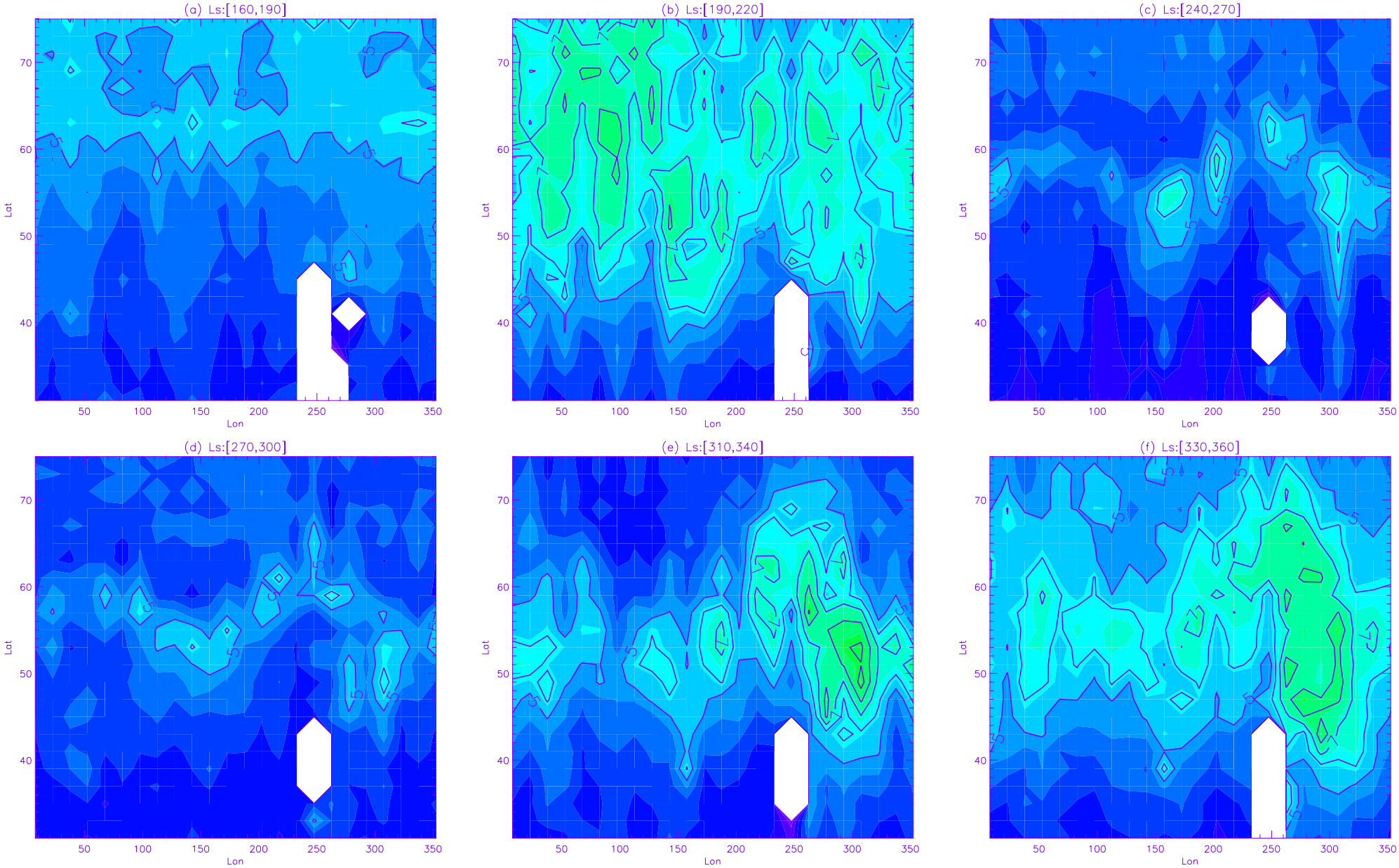
(a) Ls:[160,190]
(b) Ls:[190,220]
(c) Ls:[240,270]
(d) Ls:[270,300]
(e) Ls:[310,340]
(f) Ls:[330,360]
Lat
Lon
40
50
60
70
50
100
150
200
250
300
350

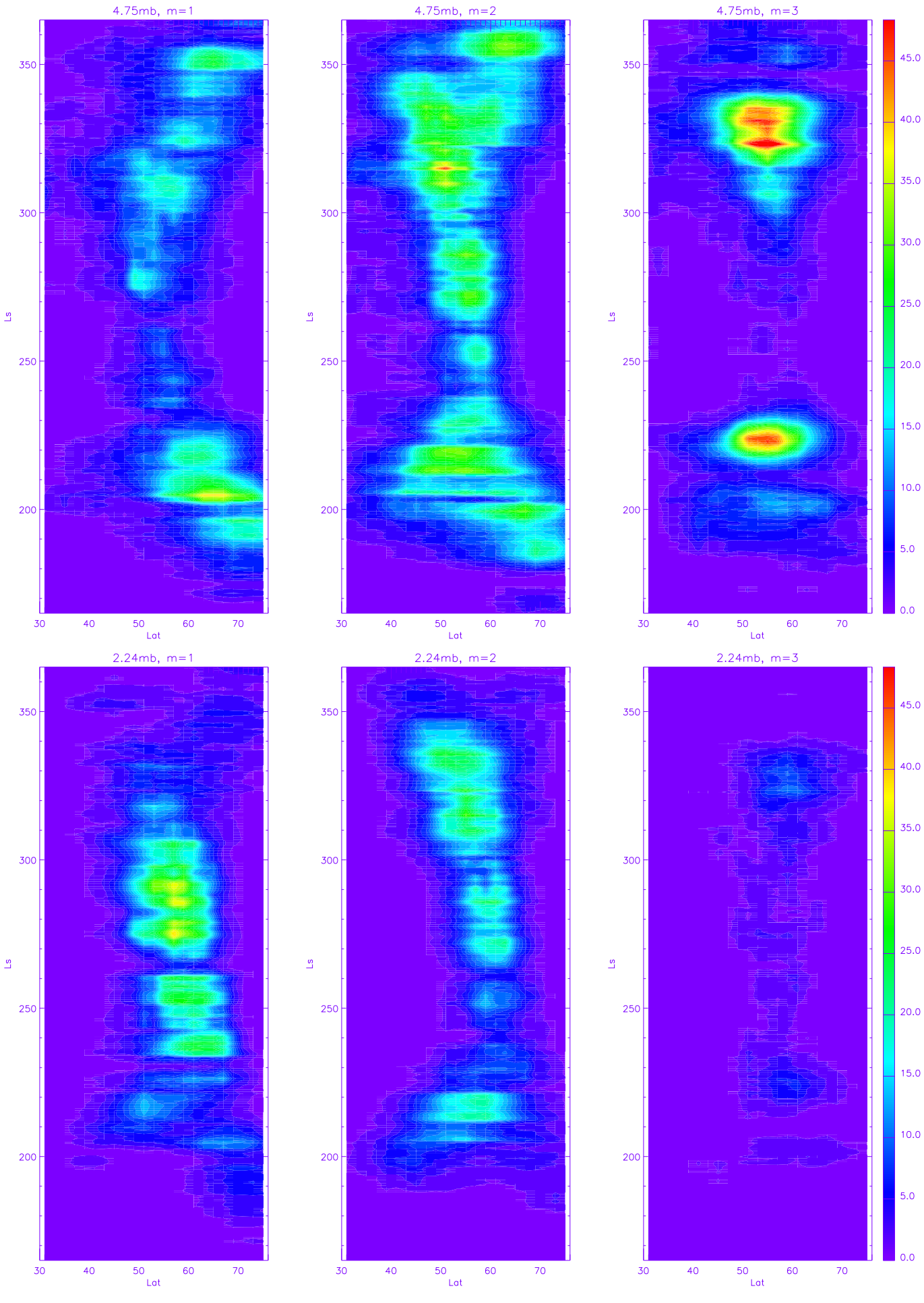
4.75mb, m=1
4.75mb, m=2
4.75mb, m=3
2.24mb, m=1
2.24mb, m=2
2.24mb, m=3
Ls
Lat
350
300
250
200
30
40
50
60
70
45.0
40.0
35.0
30.0
25.0
20.0
15.0
10.0
5.0
0.0